Substrate heterogeneity promotes cancer cell dissemination

Zuzana Dunajova[1*], Saren Tasciyan[1*], Juraj Majek[1], Jack Merrin[1], Erik Sahai[2], Michael Sixt[1#], Edouard Hannezo[1#]

[1] Institute of Science and Technology Austria (IST Austria), am Campus 1, 3400 Klosterneuburg, Austria

[2] Tumour Cell Biology Laboratory, The Francis Crick Institute, London, UK

[*]Contributed equally, [#]contributed equally

[#]Correspondence: michael.sixt@ist.ac.at, edouard.hannezo@ist.ac.at

Abstract

While tumor malignancy has been extensively studied under the prism of genetic and epigenetic heterogeneity, tumor cell states also critically depend on reciprocal interactions with the microenvironment. This raises the hitherto untested possibility that heterogeneity of the untransformed tumor stroma can actively fuel malignant progression. As biological heterogeneity is inherently difficult to define and control, we here chose a highly reductionist bottom-up approach and let tumor cells invade into micro-engineered environments harboring obstacles with precision-controlled geometry. We find that not only the presence of obstacles, but more surprisingly their spatial disorder, causes a drastic shift from a collective to a single-cell mode of invasion. Combining live-imaging and perturbation experiments with minimal biophysical modeling, we demonstrate that cellular detachments result both from local geometrical constraints and a global temporal integration of the heterogeneity experienced during the invasion process. We show that different types of microenvironments map onto different universality classes of invasion dynamics, which can quantitatively explain our findings. We thus identify generic physical principles for how the mode of cancer cell invasion depends on environmental heterogeneity, with implications to understand tumor evolution *in vivo*.

Introduction

Cellular heterogeneity is at the core of tumor evolution. The canonical view suggests that new genetic variants produce new cancer cell phenotypes that physically invade extra-tumoral micro-milieus. If these cells experience more favorable growth conditions, they clonally expand and breed new heterogeneity. In an iterative process, the tumor ultimately reaches the fatal state of systemic dissemination[1–3]. While heritable genetic variations have long been recognized to play a crucial role, phenotypic variation can also be of epigenetic nature or even result from transient signaling states[4,5]. In any case, neither variation nor selection of cancer cells are autonomous to the tumor, but follow the metazoan principle that regulation occurs in a reciprocal crosstalk with the (untransformed) microenvironment [6–8]. Remarkably, in some tumor models even invasiveness itself is an active and transient response of rare cancer cells to signals released by the benign microenvironment[9–11]. This raises the possibility that more heterogeneous extra-tumoral microenvironments act as drivers of malignancy[12], although this remains largely untested due to the difficulty of uncoupling substrate heterogeneity and malignancy *in vivo*.

In recent years, more reductionist approaches have gained increasing attention, where the behavior of cells emerges from first physical principles that do not even require genetic or epigenetic changes. For instance, bottom-up reconstitution of microenvironments have been successfully used to model cellular responses[13] and cancer dissemination in response to specific local topographies of the extracellular matrix (ECM)[14,15]. Cellular collectives can also shift between fluid and solid states as a simple function of cell-cell and cell-ECM adhesion, cell density or active migratory forces[16–22], with fluidized states favoring invasion[23–27]. Interestingly, such fluidized state can create large mechanical stresses on nuclei, which triggers mechano-adaptative responses and can thus feedback on cell malignancy to further promote invasiveness[28]. Finally, interface-dynamics of spreading tumor cell colonies display highly generic fractal-like features, that have been proposed to follow generic models for growing interfaces, such as the Kardar-Parisi-Zhang (KPZ) equation[29,30] or the Molecular Beam Epitaxy (MBE) equation[31], that have been validated in a number of non-living matter settings[32,33]. However, the above studies have all looked at migration either in homogeneous or ordered environment, so that the influence of heterogeneity of the extracellular environment remains unexplored.

Here, we pursued a reductionist microengineering-based approach to test the response of tumor cells to ordered vs. disordered environments. We chose to specifically manipulate environmental geometry, while leaving all other aspects constant, which already demonstrated complex impacts on interfacial growth and tumor dispersion. In particular, we find that cellular detachments are both impacted by local features of substrate heterogeneity, as well as a much more

global effect of temporal integration of the heterogeneity experienced by the tumor front. This led us to derive a quantitative description of the determinants of cellular dispersion, which we tested by experiments in different environments with structured geometries.

Results

Environmental mechanics and heterogeneity are sufficient to drive dispersion *in vitro*

As a cellular model for tumor invasion, we employed A431 human carcinoma cells[34]. This cell line is derived from a primary tumor of epithelial origin and forms cell-cell adhesions due to the expression of E- and P-Cadherin[35]. When plated on fibronectin-coated 2D surfaces A431 cells spread radially with a coherent cell front showing no cellular detachments from the collective (Supplementary Fig. 1a). To test invasion into geometrically precisely controlled environments, we engineered microfluidic devices where a centrally applied pool of cells spread into a fibronectin-coated confined space of 9μm height. The two confining surfaces were intersected with arbitrarily positionable 9μm diameter pillars, creating a 3D chamber that forces cells to invade as a monolayer into the “pillar forest”. The setup allowed free medium exchange, so that cells were viable and could be imaged and tracked for more than a week using genetically encoded fluorescent reporters for cytoplasm (mCherry) and nuclei (GFP). We created microfluidic chips where cells radially spread into 4 different sectors, allowing assessment of different pillar patterns under otherwise identical conditions. To test the impact of ordered vs. disordered geometries we placed pillars on grid-like patterns, creating regularly spaced obstacles that cells encounter while spreading from the center to the periphery (Fig. 1a). We chose 9μm pillar spacing, where cells could pass by only moderately deforming their ~12-18μm diameter nucleus. For disordered patterns we kept the average pillar distance constant, but randomly shifted individual distances according to a Laplace distribution (Fig. 1b). Tracking invasion over 8 days showed that cells invaded ordered patterns with occasional detachments. Strikingly, in disordered patterns cells advanced with enhanced single cell detachments at the invasion front (Fig. 1c, Supplementary Movie 1). This was in stark contrast to experiments on obstacle-free 2D surfaces, where A431 cells migrated in a highly cohesive manner in the absence of any detachment (Fig. 1d, Supplementary Movie 2). To quantify the magnitude of the dispersion effect in disordered patterns, we used A431 cells that were genetically engineered to lack E- and P- cadherin ($EPCad^{-/-}$). In collagen assays and pillar patterns $EPCad^{-/-}$ tended to invade as single cells as they moved away from the bulk, irrespective of environment geometry (Supplementary Fig. 1b-c, Supplementary Movie 3). A side-to-side comparison between wild type (WT) and $EPCad^{-/-}$ cells revealed that in disordered environments WT

101 cells showed cellular detachments comparable to EPCad$^{-/-}$ cells (Supplementary Fig. 1d). To-
102 gether, these data demonstrate that A431 cells undergo a drastic shift from collective to single
103 cell invasion when exposed to disordered geometries, with substrate heterogeneity having an
104 effect comparable to genetically inflicted loss of cell-cell adhesion.
105
106 **Minimal biophysical simulations recapitulate the effect of environmental heterogeneity**
107 Several mechanisms might explain the effect of environmental heterogeneity on single
108 cell detachments. Firstly, we reasoned that disordered pillar patterns contain regions of very nar-
109 row pore sizes, that might cause detachments by physically restricting the interfacial area of cell-
110 cell contacts. Such very small pores could also mechanically compress the nucleus, which can
111 trigger an active cellular response that might propel the cell forward, causing detachment from
112 the collective[36–41]. To test this 'pore size' hypothesis, we repeated the assay in ordered pillar pat-
113 terns with smaller spacing (6μm), requiring the nucleus to severely squeeze between obstacles.
114 We found that cells still moved collectively without increased detachment, arguing against a sim-
115 ple effect of pore size (Supplementary Fig. 1d). Next, we reasoned that gradients in pore sizes,
116 present only in disordered environments, might create detachments, as narrow constrictions fol-
117 lowed by free space might be permissive for cells at the leading edge to detach and move away
118 from the tissue bulk, which would stall in the constriction ('funnel' hypothesis). We tested this
119 option using two graded, yet ordered, pillar pattern designs, which change the pore size only in
120 the direction of cell invasion; either gradually (sinusoid design) or abruptly (stepwise design) (see
121 Supplementary Fig. 1e). Importantly, neither of these pore size variations triggered a significant
122 increase in the number of detachments (Supplementary Fig. 1f). Together, these data show that
123 cellular detachments do not simply arise from a single specific local geometry of obstacles. This
124 led us to explore other, more collective hypotheses, where detachments could result from a com-
125 plex series of transitions that the tissue experiences while passing through a disordered environ-
126 ment.
127

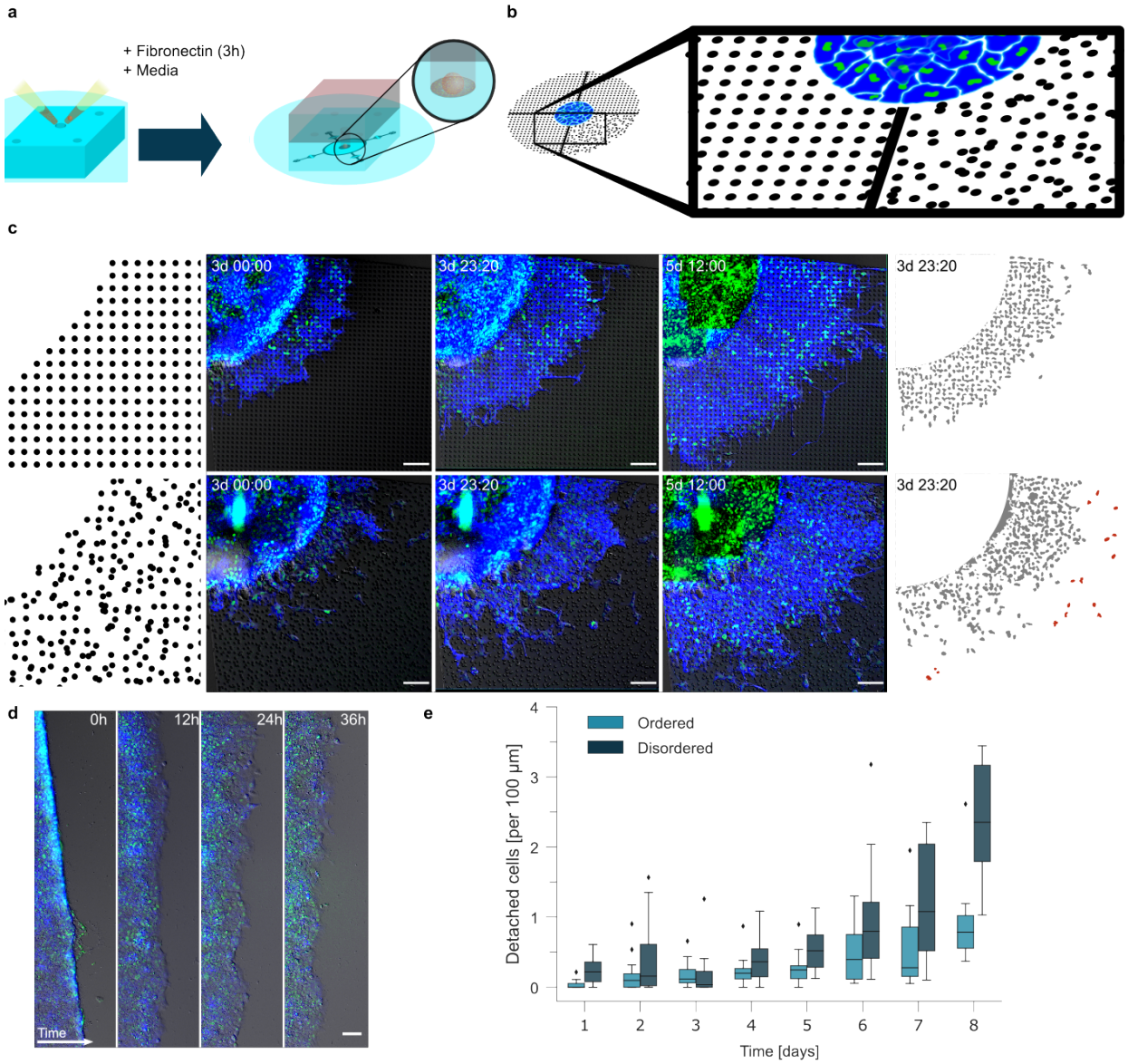

Fig. 1: *In vitro* experiments reveal a key role for substrate heterogeneity in driving tumor dispersal. **a.** Experimental setup of the microfluidic invasion assay, where surfaces are coated with fibronectin and filled with cell culture media before A431 cells are seeded into the center of the devices **b**. Illustration of the pillar patterns, where cells from the center invading into. **c.** A431 cell invasion imaged with time-lapse fluorescence microscopy over the days 3, 4 and 5.5 from left to right, where cells express cytoplasmic mCherry (blue) and nuclear H2B-GFP (green). The segmentation of the cell nuclei in day 4 is shown on the right. **d.** Scratch assays performed as a control to compare the migration of A431 cells in homogeneous environment. **e.** Number of detached cells normalized by the radial interface length in the respective pillar patterns for A431 WT. Scale bars: 100 µm, box and whiskers plot displays median, 1st and 3rd quartiles (hinges) and bars display 1.5 interquartile range from the hinges, n=16 experiments for ordered and n=18 per disordered environment, followed over 8 days.

140 For this, we turned to minimal *in silico* simulations of invasion in complex environments.
141 Cells were modeled as soft adhesive and self-propelled particles[42–45], and we assumed repulsive
142 interactions with static pillars forming patterns of different geometries (Fig. 2a). Before seeking to
143 quantitatively fit the model parameters, we first performed a broad parameter screen, and found
144 that these minimal simulations robustly reproduced key qualitative features of the data, including
145 the fact that the number of detachments drastically increased with the presence of pillars, as well
146 as with pillar heterogeneity (Supplementary Fig. 2a). We then proceeded to constrain model pa-
147 rameters in a more precise manner, to understand quantitatively what causes detachments in the
148 simulations. As detailed in the Methods (see also Supplementary Table 1 for a summary of the
149 parameter fitting), parameters related to single-cell migration properties (e.g. migration speed and
150 bias, persistence time) were inferred based on the measured behavior of single detached cells in
151 pillar patterns. Cell-cell adhesion strength was constrained based on the lack of cell detachment
152 in homogeneous environment and infrequent cell-cell rearrangements, arguing for a glass-like
153 rheology with slow re-arrangements (Supplementary Fig. 2b, Supplementary Movie 4). Simula-
154 tions ran within this parameter regime confirmed the increase of detachments induced by pillar
155 heterogeneity (Fig. 2b, Supplementary Movie 5), as well as this effect diminishing when simulating
156 cells with lower cell-cell adhesion (Supplementary Fig. 2c,d, Supplementary Movie 6), similar to
157 the experiment (Fig. 1e).
158 With this parametrization, we started by running many repetitions of simulations with a
159 specific disordered pattern and calculating a probability distribution for detachment as a function
160 of position within the pillar pattern (the analysis was based on clustering with instantaneous cell
161 positions and tracks both transient and long-term detachments). Interestingly, the most striking
162 correlation which we found was not with local position, but instead with time since the start of
163 invasion. Indeed, this analysis revealed that the probability of detachments consistently increased
164 as the cells invaded in pillar patterns, with much steeper temporal increase in disordered patterns
165 (Fig. 2c).
166

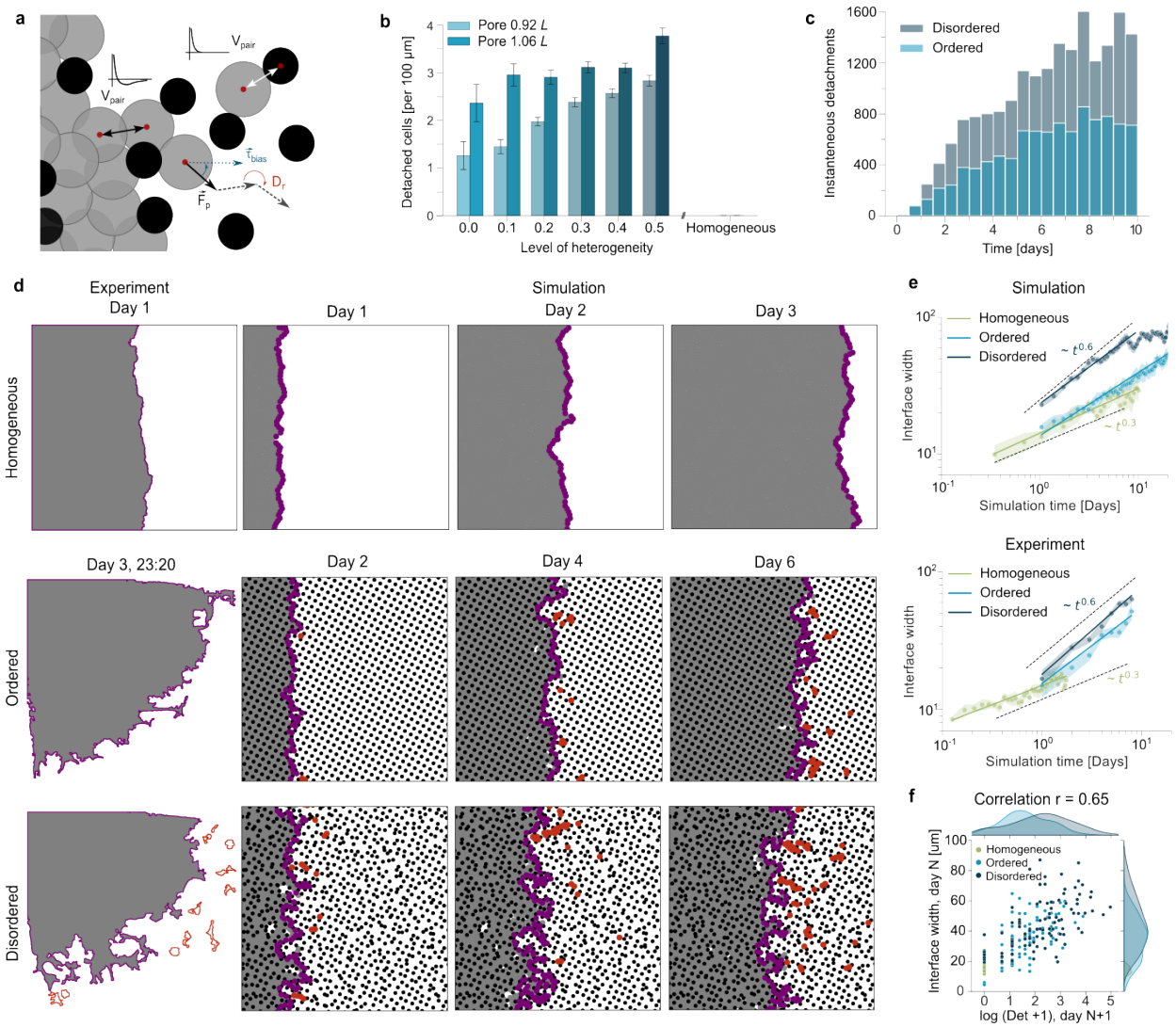

Fig. 2: Minimal particle-based simulations reveal qualitatively different dynamics of interfacial growth and detachments in different environments. a. Simulation setup of cells (modeled in grey as soft attractive particles) invading a pillar pattern (modelled in black as soft repulsive particles), with schematic description of the relevant forces and interaction potentials. **b.** Comparison of the number of detached cells (at day 6) in simulations with patterns of different levels of disorder (heterogeneity values represent parameters of Laplace distribution, see Supplementary Table 1). Bars indicate mean number of detached cells and error bars show standard error (left bar - pore size 0.92 *L*, right bar pore size 1.06 *L*). **c.** Rate of detachments are increasing in time in simulations, with steeper increase with disordered patterns. **d.** Representative snapshots at different time points of the cell interface (magenta) in simulations for different environment geometries, side by side with the cell body segmentation from corresponding experiments (see Figure 1c,d). The interface gets rougher in time and in more heterogeneous environments. Cells are shown as grey and pillars as black beads, detached cells are highlighted in red. **e.** Interface roughness in different environment geometries in simulation, showing different exponents with and

without pillars, with the steepest increase for disordered patterns ($\beta_{\text{homogeneous}}$ = 0.33, β_{ordered} = 0.46, $\beta_{\text{disordered}}$= 0.53). The markers represent the mean values, shaded area indicates the standard error and solid line the linear fit. **f.** Experimental quantification of interfacial roughness over time and for different conditions ($\beta_{\text{homogeneous}}$= 0.28, β_{ordered} = 0.55, $\beta_{\text{disordered}}$ = 0.64), showing a good agreement with the theoretical predictions. **g.** Correlation of interface width (day N) and detachment rate (day N+1) in all analyzed experiments, showing strong overall correlation over different samples and conditions (n_{ordered} = 16; $n_{\text{disordered}}$=18, $n_{\text{homogeneous}}$ = 6).

Substrate heterogeneity drives gradual roughening of the tissue interface

From a physical perspective, a classical result on the invasion dynamics of a fluid material such as a tissue is that its interface should become rougher and rougher over time and that this temporal increase follows a highly universal trend[29,46–49], which depends only on a few key characteristics of the system. This led us to the idea that cell detachments could be connected to the properties of the cell interface, and thus were sensitive to “time-integrated” heterogeneity, with each pillar passed by the invading front increasing surface roughness by a small amount. To test this, we computed in simulations both the overall perimeter of the front, which increases continuously during cell invasion (Supplementary Fig. 3a), as well as the surface roughness (i.e. deviations in the interface height with respect to its average, Fig. 2d,e). Interestingly, we found that the interface roughness always increased in time, but with different growth exponents depending on the nature of the geometrical environment. Fitting the increase to a power-law to get the growth exponent β (following conventions from statistical physics, see Methods), we found that cells migrating through homogeneous environments followed a roughness increase exponent of β=0.33. This is what is expected from KPZ dynamics, a highly universal model of interfacial growth. Strikingly, interfacial roughness in disordered patterns increased significantly faster, with a much larger exponent of β=0.5-0.6. Although initially surprising, we reasoned that this was very close to previous theoretical predictions for the so-called KPZq universality class[50–53], which describes growing interfaces in the presence of quenched disorder (Fig. 2e). Computing these exponents in our simulations for either homogeneous or disordered environments confirmed that we predict these exponents in a wide range of parameter regimes (Supplementary Table 2), despite the fact that our system is more complex than previous continuum theories, for instance due to the presence of particle adhesion and active self-propulsion.

Strikingly, computing surface roughness and exponent β in the same manner in experimental data revealed very good agreement with the data (best fit of 0.28 for homogeneous and 0.64 for disordered environments). Furthermore, in simulations of ordered pillar patterns, we

found that the predicted growth exponent depends on the average pore size as well as orientation of the pattern relative to the direction of cell invasion (Supplementary Table 2, Supplementary Fig. 3b,c), but is mostly found to be intermediate between homogeneous and disordered, with systematically lower interface width compared to disordered environments. This was verified in the experimental data, where we found a roughness exponent of 0.55 for ordered environments with an interface width that was on average 21% lower in ordered compared to disordered environments. Once we could rationalize the dynamics of interfacial growth in different environmental conditions within this simple general model, we asked whether this could explain the different trends of temporal increase in detachments across conditions. For this, we correlated at each time point, for a given experimental replicate, the interface roughness at day N with the number of detachments at day N+1. Strikingly, we found a strong correlation (R^2=0.65) across all data points and different conditions, arguing that there might be a causal link between interfacial roughening and cell detachments (Fig. 2f). To test further this theory, we went back to aforementioned geometries which did not trigger detachments, such as ordered patterns with small pore size and sinusoid or stepwise designs (Supplementary Fig. 3d, Supplementary Movie 7). Running simulations in the same parameter regime, but corresponding pillar geometries, demonstrated good agreement with experimental data, as we could predict both lower interfacial roughness and lower number of detachments in all of these conditions compared to random pillars (Supplementary Fig. 3e).

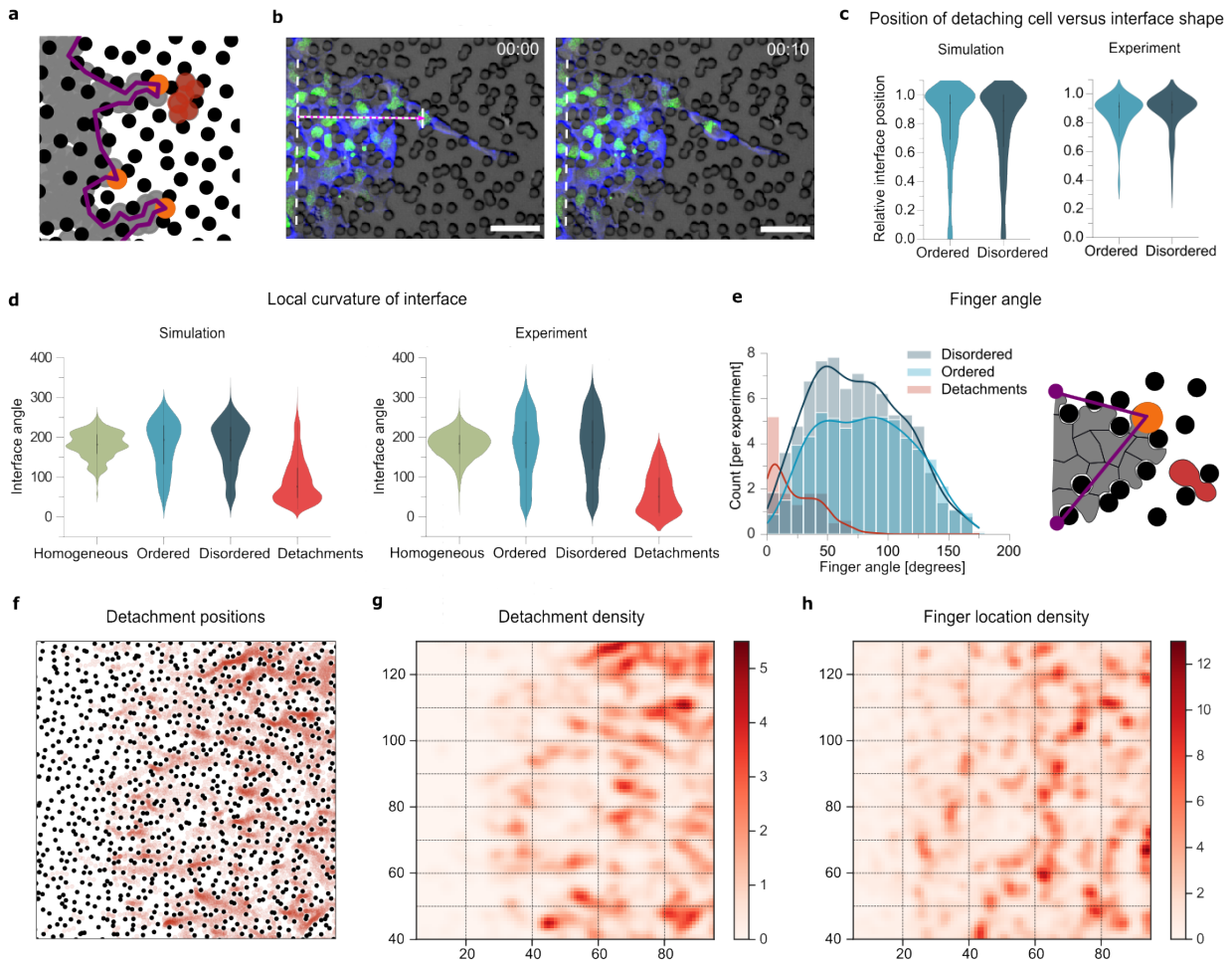

Fig. 3: Predicting detachment dynamics from interfacial roughness across conditions. **a.** Details of the interface shape (magenta) analyzed in simulations. The cells are shown as grey and pillar as black beads, tips of interface protrusions are highlighted in orange, detached cells in red. **b.** Illustration of the measurements of position of detaching cell relative to interface shape, where the distance from the protrusion baseline and tip of protrusion is normalized. The measurement is performed in the last frame before detachment. Cell bodies were expressing cytoplasmic mCherry (blue) and nuclear H2B-GFP (green). Scale bar, 100μm. **c**. Relative position of the detachments compared to the finger baseline (0: at local minimum, 1: at the tip of the fingers). Middle line, upper and lower lines indicate the median, first and third quartiles, respectively (collection of n=100 detaching cells from n=7 experiments and n>700 from n=40 simulations for each condition). **d.** Local curvature of the interface in homogeneous, ordered and disordered environments, and local curvature of interface at detachment positions (n=6 experiments with homogeneous, n=16 for ordered and n=18 for disordered environment, n=40 simulations for each condition). Pillar patterns, especially the disordered pattern exhibit higher pool of interface positions with curvature high enough for the cells to detach. **e.** Aspect ratio of the interface protrusions (angle between tip of the

interface and “shoulders”, ie. next local minima) in experiments. Disordered environment generates pattern with higher number of long, narrow fingers. Same dataset was used as in d). **f-h.** Statistics of the distribution of interfacial protrusions (g) and detachments (h) across n=10 simulations with the same disordered pillar pattern (f), confirming that the location of interface protrusion is highly predictive of detachments (R^2=0.6).

Quantitative local and global determinants of cellular detachments

To follow up on this finding, we sought to study more precisely how a global property such as interface roughness is linked to a local property such as cell detachments. We hypothesized that a rougher invasion front leads to formation of interface regions with higher curvature and fewer cell contacts, which might facilitate detachments[54–56]. Indeed, when we analyzed individual detachment events in simulation and experiment, we found that the cells most likely to detach were located at the tip of convex “finger-like” protrusions of the interface (Fig. 3a-c). Accordingly, we analyzed local curvature of the interface shortly before the detachment (which negatively correlates with the local number of cellular neighbors) (Fig. 3d), and we found that the majority of cells detached from interface positions above a threshold curvature value. Interestingly, cells migrating in pillar-free environments never reached such high interfacial curvature values, providing a quantitative explanation for their lack of detachment. While there was no striking difference between the curvature distribution of ordered and disordered patterns in experiment, which could be due to the difficulty of segmenting extremely rough interfaces (Supplementary Fig. S4a), we found that the aspect ratio of the fingers in disordered patterns was significantly higher than in ordered patterns, and increased towards later time points (Fig. 3e, Supplementary Fig. 4b), which again supports a close relationship between detachments and local interfacial curvature created by the heterogeneous environment (Fig. 3f-h, Supplementary Fig. 4c). Overall, our findings support the idea that invasion into pillar patterns is a cumulative phenomenon. It results in a gradual increase of interfacial roughness over time, with different exponents and slopes depending on environmental geometry. The existence of a critical roughness which is permissive for detachments explains that detachments do not occur at early time points in the presence of pillars and never appear in the absence of pillars (at least within our experimental time).

To test this further via independent experiments, we designed new pillar geometries, characterized by sinusoid patterns perpendicular to the direction of invasion. By making the sinusoidal modulation relatively mild, we ensured invasion across the entire pillar pattern, but with a controlled curvature modulation (Fig. 4a, Supplementary Movie 8). As predicted by the simulations, this geometry promoted formation of periodic finger-like protrusions in the regions of maximal

pore width (Fig. 4b), as well as higher detachment probability with increasing frequency of sinusoid modulation, resulting in sharper fingers (Supplementary Fig. 4d). In both simulations and experiments, the average probability of detachments scaled with the local interface shape (Fig. 4b-c, e-f).

Finally, we asked whether there were additional local geometrical predictors for detachment, on top of such global integrated heterogeneity. Indeed, as discussed above, simulations repeated over the same disordered geometry revealed locations where more detachments occurred. Given that we found that sinusoidal patterns parallel to the direction of invasion did not yield detachments (Supplementary Fig. 1d-e, 3c-d), whereas sinusoidal patterns perpendicular to the direction of invasion did (Fig. 4a-c), we specifically computed different metrics for local pillar anisotropies in the front, back or sides of the invasion direction (Fig. 4g, Supplementary Fig. 4e-f). Interestingly, we found in simulations that regions with locally anisotropic free space (i.e. less pillars in the direction parallel to invasion compared to perpendicular) displayed a small but significant correlation with detachments (R^2=0.1). By combining this metric of local pillar anisotropy together with the long-term trend of roughness-induced increases in detachment, we could achieve good predictive power for the spatiotemporal statistics of detachments in simulations (R^2=0.64, Supplementary Fig. 4e). To confirm this, we followed individual cell trajectories in simulations, and found that increased pillar anisotropy was observed specifically at the time of detachments (Fig. 4h). To test this experimentally, we computed the local anisotropy of pillar geometry across n=94 cellular trajectories with detachments, and found indeed a statistically larger number of pillars perpendicular compared to the parallel direction of movement at the time of detachment (Fig. 4i). Together, our data show that a geometrically disordered environment promoted detachments primarily via globally increased interfacial roughening, with finger-like regions of high curvature, but that, in addition, local substrate anisotropy tunes the likelihood of cell detachment.

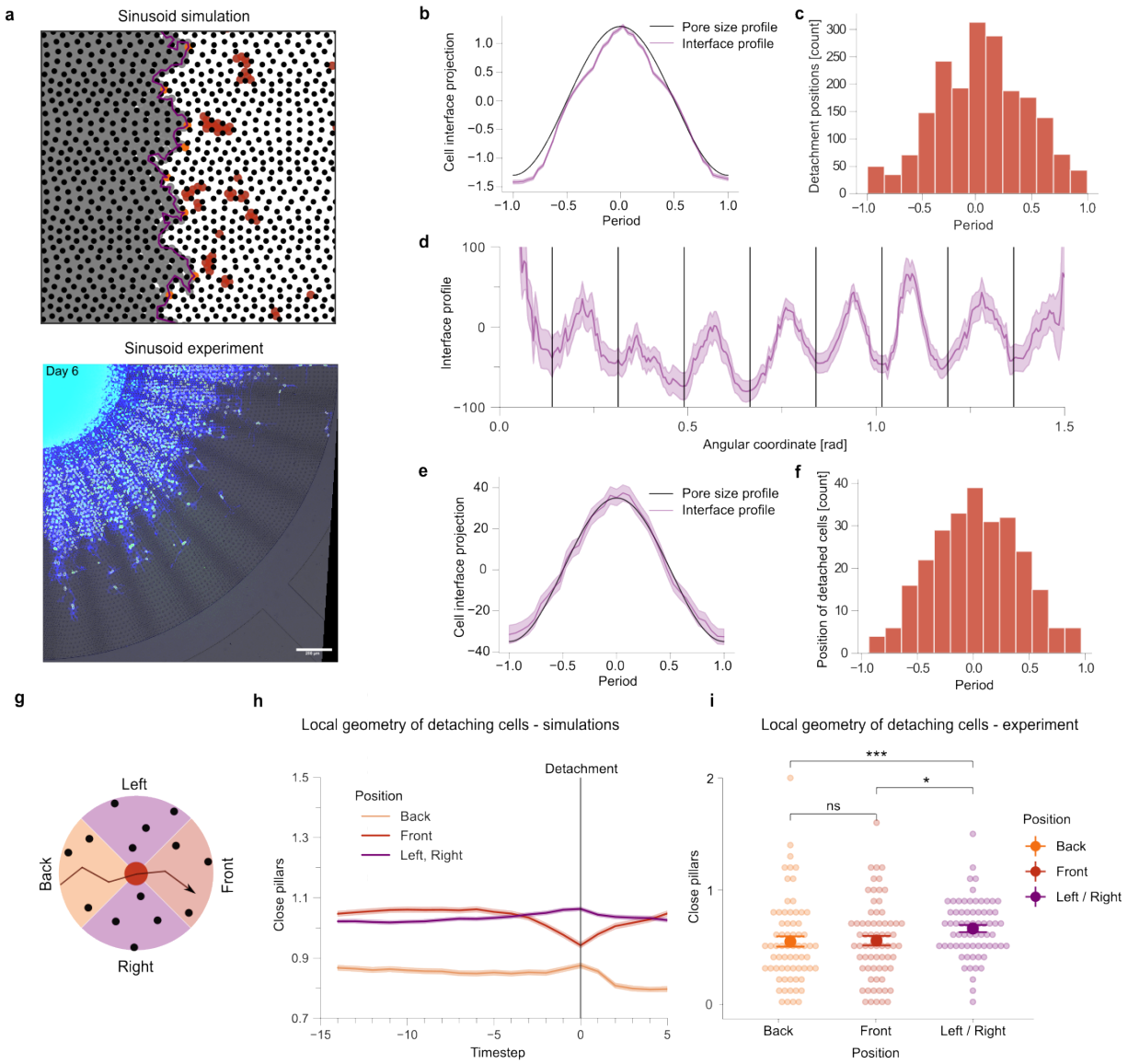

Fig. 4: Predicting the statistics of detachments as a function of global and local heterogeneity. **a.** Simulation and corresponding experiments of cells in longitudinal sinusoid pillar pattern featuring only lateral heterogeneity of pore size. Cells invade with forming regularly spaced finger-like protrusions. Top panel: simulation at day 6, cells are represented as grey and pillar as black beads, finger maxima shown in orange, cell interface in magenta, detached cells in red. Bottom panel: experiment, cell bodies were expressing cytoplasmic mCherry (blue) and nuclear H2B-GFP (green). **b.** Interface profile in simulations (purple line, shaded area indicates standard error, n=10 simulations), averaged over all timepoints and multiple periods of the sinusoid pore size profile, showing that interface position correlates strongly with regions of low pillar densities. **c.** Instantaneous detachment positions in simulations collected from all timepoints and periods of sinusoid pore size profile. **d.** Interface profile in experiment averaged over all timepoints in spherical coordinates (shaded area indicates standard error, n=4 experiments). **e-f.** Averaged interface profile

(e, purple line, shaded area indicates standard error) and position of recently detached cells (f, red bars), which match well the prediction of simulations (see resp. panels b and c), n=4 experiments. **g.** Schematics for how local features of pillar geometry are quantified (see Methods). At each point in space, nearby pillars are divided into 4 quadrants – front, back, left and right, and we compute different statistics for how the pillar density in each quadrant correlates with detachments. **h.** Local pillar geometry along the trajectory of detaching cells in simulations (time=0 at detachment, n > 10000 detachment events from 40 simulations). As the cell is going to detach, the number of pillars in front of the cell decreases and increases on the sides of the cell (leading to detachments in locally anisotropic regions). **i.** Experimental number of pillars at the time point of detachment in different quadrants (dot plot and error bars display mean and standard error from the mean, collection of n=68 detaching cells from n=7 experiments, P 0.0045 (Back vs. Left/Right), 0.018 (Front vs. Left/Right) and 0.74 (Back vs. Front), Wilcoxon test), showing a statistically significant increase in side pillars (increased local anisotropic), as predicted experimentally.

Discussion

Our results demonstrate the importance of environmental heterogeneity in the dissemination of cancer cells and illustrate the crucial role of invasion interface shape in this process, an intrinsically collective tissue property. We find that substrate heterogeneity drives cell detachments from the bulk in a non-trivial way, acting via two complementary mechanisms. As cells go through a disordered environment, the free invasion interface gets gradually rougher, effectively integrating heterogeneity over time. We expect that this is a highly generic effect, as we show that we can map the dynamics of interfacial roughening to a generic universality class of active physical processes (KPZq). After a critical amount of time, the interface roughness is large enough that cells at the tip of invading fingers have few enough neighbors to detach. This permissive, integrated effect is then compounded by the local substrate geometry, which selects specific sites of local anisotropy where detachments are specifically promoted.

Although we have investigated this in an *in vitro* setting, where environmental geometry could be finely tuned, a next step would be to quantitatively compare our findings to more realistic *in vivo* situations[57]. For instance, different organs have different organization of extracellular matrix[58], which seem to sit between fully ordered and fully disordered states, although this has not been systematically quantified. Generalizing our simulations to tumor invasion in a 3D fibrous environment could lead to key insights to understand the influence of tissue-environment cross-talk in invasion dynamics. In line with that idea, quantitative imaging of human tumor samples revealed that spatially disordered or tilted stromal compartments can be negative prognostic factors for clinical outcome[59,60]. Another natural extension of the model would be to consider remodelling of the environment due to mechanical forces exerted by cell migration[61].

357 Using an experimentally controlled bottom-up approach, we introduce stromal heterogeneity as a potential driver of malignant progression. In analogy to organismal evolution, where more heterogenous habitats drive genotypic diversity, a more heterogenous tumor stroma might shift tumor cells into novel phenotypic states (in our case, the single cell as opposed to the collective state). Despite being transient phenotypes without heritable traits, these states might later become consolidated[28] by epigenetic and ultimately genetic accommodation.

Acknowledgments

The authors thank all the members of the Hannezo and Sixt groups for fruitful discussions and Takuya Kato for advices on the experimental set-up. We are also thankful for support from the Scientific Service Units (SSU) of IST Austria through resources provided by the Imaging and Optics Facility (IOF) and the Lab Support Facility (LSF). Z.D. has received funding from the Doctoral Programme of the Austrian Academy of Sciences (OeAW): grant agreement 26360. This work was supported by the European Research Council (grant ERC-SyG 101071793 to M.S).

Author contributions

S.T., Z.D., M.S., and E.H. designed the research. S.T. performed the experiments: S.T., Z. D. and Ju.M. performed data and image analysis; Z.D. and Ju. M. performed simulations; Ja.M. supported microfluidic engineering; E.S. provided cellular model systems. M.S. and E.H. supervised the study; S. T., Z.D., M.S. and E.H. wrote the manuscript, with input from all authors.

Methods

Experiments

Cell Culture

A431 cells expressing mCherry were grown in DMEM (Gibco, 10569010) containing phenol red, high glucose, GlutaMAX, pyruvate, 10% fetal calf serum (FBS, Gibco, 10270106), non-essential aminoacids (Gibco, 11140050), penicillin (50U/ml) and streptomycin (50µg/ml, Gibco 15070063) in humidified incubators at 37°C with 5% CO_2. EPCad$^{-/-}$ A431 cells were made as described in Labernadie et al. 2017[62]. Cells were regularly tested for mycoplasma contamination and preserved in growth medium containing 5% (v/v) DMSO in cryogenic conditions for longer periods.

387 Cells were transfected with lentivirus containing H2B-GFP construct and selected for blasticidin
388 resistance and then later sorted for GFP signal, regularly.

389 Device Fabrication

390 Patterns were generated with Python script in SVG format. Designs of photomasks were com-
391 pleted in (Inkscape, v0.92) in layers for each confinement. SVG files were converted to AutoCAD
392 DXF R14 files, further converted to Gerber files (LinkCAD) and finally printed on chrome photo-
393 masks at a resolution of 1 µm (JD Photo Data & Photo Tools). For high-resolution structures,
394 wafers were first coated with a sub-micrometre layer of SU-8 as a sticky substrate for later SU-8
395 structures. We used GM-1040 SU-8 photoresist (Gersteltec) at 5,000 rpm for 2 min with flood UV
396 exposure. The feature layer was then applied with SU8-2005 (Microchem). According to the
397 datasheet, a UV-absorbing glass plate and higher exposure were used to make sharp features.
398 PL-360-LP from Omega Optical and 550 mJ/cm^2 with an EVG mercury lampbased mask aligner
399 gave good results in the 3–9-µm-thickness range. The thick (25 µm) loading channels were made
400 with Microchem SU8-3025 using the EVG mask aligner according to the Microchem data sheet
401 without the PL-360-LP plate. The master wafers underwent vapour silanization for 1 h with (1H,
402 1H, 2H, 2H-perfluorooctyl) trichlorosilane. The final results were single hydrophobic master wa-
403 fers containing several aligned layers. Polydimethylsiloxane (PDMS) devices were made with Syl-
404 gard 184 Elastomer Kit (Dow Corning) using a ratio of 10:1. The PDMS was mixed in a Thinky
405 mixing machine and then poured on the wafer in a 3D printed tray and further degassed several
406 times in a vacuum chamber. The devices were baked at 80 °C overnight. The hardened devices
407 were carefully peeled off the mould and cut into single devices using a razor blade. Holes were
408 punched with a custom arbor press or with skin biopsy puncture tools (1 mm) for the central hole,
409 and sticky tape was used to remove debris. Glass coverslips were sonicated for 5 min in 100%
410 isopropanol and blown dry. Devices were bonded to the glass slides by oxygen plasma then
411 sealed together at 85 °C for 1 h to make the bond permanent.

412 Invasion Assays

413 Microfabricated devices were inserted into 12-well cell culture plates from the bottom side and
414 glued with molten paraffin. Devices were filled with fibronectin (F1141, Sigma) solution (diluted in
415 1:5 from 1mg/ml stock solution in PBS) using a syringe pump, sealed and incubated for 3h in cell
416 culture growth conditions. Devices were later flushed with 100 µl cell culture growth medium with
417 syringe pumps. Debris were removed from the center hole, either spheroids of cancer cells (gen-
418 erated with hanging drops) were dropped or a pipette tip filled with medium was inserted into the

419 hole, where 1.5 µl of the cell suspension was filled. Cells were incubated until they sank into the
420 hole and imaged at later days. Wells were checked for contamination under microscope.

421 2D Spread Assay

422 A431 cells were mixed with cytoplasmic mCherry reporter expressing A431 cells (10:1) and as-
423 sembled into 1000 cell spheroids in hanging drops overnight. Glass cover slips were coated with
424 fibronectin (F1141, Sigma, diluted in 1:40 from 1mg/ml stock solution in PBS) for 1h and then
425 washed with PBS. Subsequently, chambers were filled with cell culture media and spheroids were
426 placed to adhere on the substrate. Cells were observed with fluorescence and DIC microscopy.

427 Scratch Assay

428 In order to observe invasion on non-confined 2D surface with an initial straight interface, cells in
429 suspension were placed and grown to full confluence on fibronectin coated glass substrates (see
430 2D spread assay above). Then, approximately at the center of the cover slip, cells were scratched
431 with a rubber cell scraped and detached cells were aspirated and washed away with cell culture
432 media. Cells were observed with fluorescence and DIC microscopy.

433 Imaging

434 Cells were either imaged once a day at room conditions or in cell culture conditions for time-lapse
435 imaging (10 min interval) for several days (typically 3-4 days). Invasion was recorded with an
436 inverted wide-field Nikon Eclipse Ti-2 microscope equipped with a Lumencor light source (475
437 nm for GFP and 594 nm for mCherry) and an incubation chamber, heated stage and CO_2 mixer
438 (Ibidi). Generally, the fluorescence imaging was accompanied with light microscopy (DIC) imag-
439 ing. For long term imaging, phenol red color was checked and the temperature was monitored
440 with a temperature sensor. Custom made CNC milled box and a pair 3D printed plugs were used
441 to prevent CO_2 and humidity leak.

442 Collagen Assay

443 A collagen mixture was created with a final collagen concentration of 1.7 mg/ml by mixing bovine
444 collagen (PureCol, Advanced BioMatrix) in 1x minimum essential Eagle (Sigma) and 0.4% sodium
445 bicarbonate solution (Sigma Aldrich). Mixture was checked for a pale pink color to ensure for
446 correct pH for polymerization. 20 µl of the collagen mixture was mixed with 9 µl of the growth
447 medium and mixed gently. Subsequently, 1 µl of the spheroid containing growth medium was
448 added to the mixture and mixed by stirring with the tip. Final mixture was gently placed on a glass

449 coverslip, which was previously glued under a 60 mm dish with molten paraffin. The dish was
450 flipped to let the collagen drop hang from the glass coverslip, whereas the plastic lid was filled
451 with droplets of PBS to keep the dish humidified inside the incubator. Collagen drop was let to
452 polymerize in the incubator for 45-60 min under cell culture conditions. Before imaging, PBS was
453 removed and the dish was flipped again and medium was added to the chamber with the collagen
454 drops. Invasion into the collagen was imaged with light microscopy (DIC) over several days under
455 cell culture conditions.

456 Lentivirus Production

457 Lentivirus production was performed as described previously[63]. In brief, LX-293 HEK cells (Clon-
458 tech) were co-transfected with LentiCRISPRv1 or LentiCRISPRv2, packaging-ps-PAX2 (Addgene
459 no. 12260) and pCMV-VSV-G envelope plasmids using Lipofectamine 2000 (ThermoFisher Sci-
460 entific) as recommended by the manufacturer, and cells were resuspended in the growth medium
461 1 day before transfection. Supernatant was collected after 72 h and stored at −80 °C.

462 Image processing and experimental analysis

463 Image Analysis

464 FiJi was used for image processing, including using the TrackMate plugin for manual cell track-
465 ing[64,65]. Proprietary ND2 files from Nikon NIS Elements were converted using Bio-Formats plugin[66]
466 and the physically calibrated (pixel size and imaging interval). Images were aligned and pro-
467 cessed into TIFF and HDF files. Most of the analysis processes were automated with ImageJ
468 macros. Cell nuclei (H2B-GFP, green) and the remaining cell body (mCherry, blue) and nuclear
469 H2B-GFP (green) were initially segmented using Ilastik and then particle analysis feature was
470 used to quantify invasion[67]. Cells were tracked semi-automatically with TrackMate, tracks were
471 corrected manually. Dividing and dying cells were excluded, all gaps were filled with interpolation.
472 Final images were processed with automated scripts for display and exported into PNG. In im-
473 ages, cells were considered detached, when their cell bodies were not considered touching the
474 bulk. Finger measurements were performed manually by measuring the distance from the tip to
475 the finger baseline. Detachments were selected over a wide range of recorded experiments. The
476 pore size of the detaching cell during detachment vs. the pore size in front of the cell, which is
477 being detached from, was measured manually with an interactive macro.

Experimental data analysis

The cell interface in experiment was obtained by identifying the nuclei positions of cells at the interface, for better comparison with simulations, which do not model the cell bodies (Supplementary Fig. 4a). Identification of cells at interface was done by first running Delaunay triangulation of all cell nuclei in each timestep and subsequently removing the vertices, which cross through the segmented interface of bulk cell bodies (blue line in Supplementary Fig. 4a). This way we could efficiently find all cells, which are in contact with the very rough and irregular bulk interface. Before using the interface positions for analyzing the roughness exponents, we had to remove the overall tilts in the interface present in some experiments (see left panel in Fig. 1d, Supplementary Fig. 5a). This was done by removing long-wavelength Fourier modes (> 500 μm). The analysis of the local pillar geometry around the detaching cells (Fig. 4i) was performed by identifying all close pillar in a given radius around a the x,y position of the detaching cells and dividing them into 4 quadrants (front, back, left right, see Fig. 4g, the center of the front quadrant being the orientation of the detaching cell). Multiple radii were tested, all resulting in qualitatively similar result (final value: r_{max}= 27 μm, i.e three times the pore size). The identified pillars in each quadrant were subsequently weighted by their distance from the reference position $(r_{max}-r)/r_{max}$ and summed.

Statistics and Data Visualization

All statistics for experimental data were performed in *R (4.0.3)* and plotted using *ggplot2* package (R Core Team 2020; Wickham 2016:2). Tracking data was analyzed with *TraXpert*, an in-house developed particle tracking analysis application. Directionality data was analyzed with *circular* package and circular statistics[68,69]. Minor cosmetic adjustments were performed in *Inkscape*, without affecting the data points or the interpretation of the plots. Figures were assembled in *Inkscape* and exported into high resolution lossless PNG images.

Numerical model

We used two dimensional Brownian dynamics simulations as a minimalistic model of collective cell migration[42–45] through complex environments (Fig. 2a). Each cell is represented by a soft self-propelled particle (representing its nucleus[39]) on a substrate, so that the overdamped equation of motion for each particle reads:

$$\gamma \frac{d\vec{r_i}}{dt} = \frac{dV_{pair}}{dr_{i,j}} + \vec{F_p}$$

where γ is the friction coefficient, $\vec{r_i}$ are the coordinates of the particles, V_{pair} is the pairwise interaction potential, and $r_{i,j}$ is the distance between particles. $\vec{F_p}$ is the active self-propulsion force acting along the particle orientation $\vec{p}_i = (cos\theta_i, sin\theta_i)$ which in the absence of any interactions, would result in an average cell speed of v_0, such that:

$$\vec{F_p} = \gamma v_0 \vec{p}_i$$

The polarity of migrating cells is affected by rotational diffusion and is additionally biased by an external torque τ_{bias}, which represents the cues which drives cell migration away from the bulk (see below for additional discussion of the source of this external cue):

$$\frac{\delta\theta_i}{\delta t} = \tau_{bias} + \sqrt{2D_r}\eta = -k_{bias}sin(\theta_i) + \sqrt{2D_r}\eta$$

Here, D_r is the rotational diffusion coefficient, η is a unit variance random variable, k_{bias} parameter describing the strength of the biasing torque, where $\theta_i = 0$ represented the direction of the invasion (right-hand side of all simulations shown here). To validate the numerical implementation, we calculated the mean square displacement of a single active Brownian particle without the biasing torque[70]. The detected crossover between ballistic and diffusive behavior was consistent with the used value of D_r.

To describe cell-cell interactions, we assume a simple potential with short range repulsion and middle range attraction[42,43,71] with the form

$$V_{pair} = \sum_i \sum_{j>i} v_{pair}(r_{i,j})$$

$$v_{pair}(r_{i,j}) = \begin{cases} 4\epsilon\left[\left(\frac{\sigma}{r_{i,j}}\right)^4 - \left(\frac{\sigma}{r_{i,j}}\right)^2\right] + \Delta \mathrm{v}_{\mathrm{pair}}(r_{i,j}) \ , & r_{i,j} < r_{cut} \\ 0, & r_{i,j} \geq r_{cut} \end{cases}$$

where $r_{i,j}$ is the distance between the positions of particles *i* and *j*, ϵ is the depth of the potential well, σ is the characteristic distance of interaction and r_{cut} is the cutoff distance of the potential. The potential is shifted by a linear pair potential Δv_{pair}, to ensure that the potential and its derivative smoothly goes to zero at the cutoff $\frac{dv_{pair}}{dr}(r_{cut}) = 0$.

Furthermore, to represent the complex environments that cells migrate in (pillar geometry), we also positioned stationary particles into the simulation box, which contribute to the total pair potential. The cell-pillar interaction is truncated at its minimum ($r_{cut} = \sqrt{2}\sigma$) to account only for repul-

535 sive interactions, given that we find no strong evidence of cell-pillar adhesion. An important as-
536 sumption of our minimal modeling approach is that cellular parameters are the same across con-
537 ditions, with differences only arising from substrate heterogeneity.

538 Details of the simulation setup

539 We used HOOMD-blue v3 library to run the numerical simulations[72]. The equations of motion
540 were numerically integrated using the Euler-Maruyama scheme with timestep dt =0.001τ. The
541 simulations are performed in two dimensions.
542
543 Simulation parameters and results are reported in dimensionless form. For convenient compari-
544 son to experiment the length is measured in units of cell-cell equilibrium distance L (defined as
545 the interaction minimum $1L = \sqrt{2}\sigma$ = 16 um) and time τ = 10^3 s. The simulation output is saved
546 every 600 frames, consistent with the smallest timestep in experiments (10 minutes).
547
548 Unless stated otherwise, the simulation parameters to model are summarized in the Supplemen-
549 tary Supplementary Table 1:
550
551 **Supplementary Table 1:** Summary of the used simulation parameters.

Parameter	Notation	Chosen value (simulation units)	Parameter fitting
Friction coefficient	γ	1	fixed parameter, non-dimensionalizes timescales
Attraction cutoff	r_{cut}	1.55 L (1 L for cell-pillar interaction)	fixed parameter (on the order of cell size, to avoid next neighbor interactions)
Self-propulsion speed	v_0	0.43 L/τ	fitted to correspond to mean single cell speed 6.9*10^{-3} μm/s inside the pillar pattern (Supplementary Fig. 5a,b)
Rotational diffusion	D_r	0.7 τ^{-1}	fitted according to MSAD of the experimental trajectories of detached cells (Supplementary Fig. 5c)
Bias torque	k_{bias}	0.75 rad/τ	fitted according to the drift of experimental trajectories of detached cells

			(Suplementary Fig. 5d)
Cell fluidity number	$\gamma v_0/\varepsilon$	0.52	constrained by confluency of cells, while keeping occasional cell rearrangements of bulk (Supplementary Fig. 2b, Supplementary Movie 4, Supplementary Table 3)
Pore size	L_p	0.88 -1.3 L	free parameter (on the order of cell size, lower bound is set that cells need to be able to pass the pores alone)
Pore heterogeneity	$\mathcal{H}$	$\mu = b = 0.1*L_p$ - $0.5*L_p$	defined by parameters of Laplace distribution, upper bound taken from disordered pattern in experiment

Before doing a systematic parameter search, we first constrained parameters to reasonable values and performed non-dimensional analysis to identify the key dimensionless ratios. The fluidity of a tissue in the absence of any obstacles is governed by a dimensionless number relating self-propulsion and cell-cell interaction strength ($v_0\gamma/\epsilon$)[44,73,74]. If the ratio is too low, cells behave as solid with very few rearrangements of neighbors, while above a given value, the tissue fluidizes as motility-driven re-arrangements become possible. However, when considering not only bulk tissue, but also a cell interface, very large values of this ratio also cause spontaneous detachments of cells in pillar-free environment as in a gas[75]. Importantly, experiments of monolayers invading homogeneous environment support an intermediate value of the ratio, as we observed virtually no detachments, but that cells could move relative to one another (Supplementary Fig. 1b, Supplementary Movie 4, Supplementary Table 3).

Furthermore, we can take advantage of the presence of single detached cells in experiments with pillars to constrain a number of parameters related to single-cell migratory properties. In particular, by calculating instantaneous (x,y) displacements and mean squared angular displacement (MSAD)[76] of detached cells in pillar patterns in simulations and experiments, we could strongly constrain the values of both self-propulsion speed and particle persistence length v_0/D_r (Supplementary Fig. 5b-d). The value of external bias was fixed by analyzing the radial drift in the trajectories of detached cells in experiment and compared to simulations (Supplementary Fig. 5e). Note that we detected a strong biased migration even in single cells far from the leading edge, which motivates the fact that this bias doesn't simply arise from pushing forces from bulk proliferation.

Given previous reports of self-generated gradients guiding long-range migration[77,78], such mechanisms would be compatible with this bias, which we chose to be agnostic about in the simulations. Finally, we performed an additional sanity check by comparing mean squared displacement (MSD) of single detached cells in simulation and experiment, allowing us to verify the chosen the combination of parameters D_r, v_0, and k_{bias}. We achieved a reasonable fit, especially for long times (Supplementary Fig. 5f).

The simulations of migrating cells used for comparative statistics in various pillar geometries and parameters (Fig. 2b, Supplementary Fig. 2ab, Supplementary Fig. 5, Supplementary Table 2) were initialized with a rectangular box of size Lx=Ly=425 L. The left part of the box was filled with cells in hexagonal packing, while the right side contained the pillar geometry. Simulations used for close temporal comparison with experiment (Fig. 2c-e, Fig. 3-4, Supplementary Fig. 3-4) were initiated in a smaller box (Lx=425 L, Ly=106 L) with new cells being added on the left side of the box during the simulation run to maintain a stable pressure in the bulk. Each combination of parameters was run with at least 10 repeats. The ordered pillar geometry was constructed as square packing with pillar spacing being twice the effective pillar diameter. The reported results of ordered pattern simulations (e. g. Fig. 2b,c,e and Fig. 3d) are averaged over 4 orientations of the square spacing (0, 15, 30 and 45 degrees, see Supplementary Fig. 3b). The disordered pattern was created from ordered patterns of all 4 tilts by shifting each pillar in a randomly chosen angle by distance following Laplace distribution from the original positions (fully disordered pattern corresponded to Laplace distribution parameters $\mu = b = 0.5 * L_p$).

Simulation analysis

The initial time needed for the cells to accumulate at the front of the pillar pattern and enter it was discarded in the analysis. Unless stated otherwise, simulation frames were analyzed with frequency 6 τ after the start of the invasion. The simulations were run until the bulk cells reached the end of the pillar pattern. The simulation analysis was performed in Python.

The overall number of detached cells (Fig. 2b,d, Fig. 3a, Supplementary Fig. 2a,c, Supplementary Fig. 3d) was analyzed by distance clustering of cells (r_{cut} was used as the natural clustering cutoff from the physical point of view) and summing the number of cells inside of the pattern, which are not connected to bulk in a given timepoint. The identification of the pattern locations with high detachment probability and instantaneous detachments (Fig. 2c, Fig. 3c-d,f-g, Fig. 4c,h, Supplementary Fig. 2d, Supplementary Fig. 3e, Supplementary Fig. 4c-e) was performed by first running

the same clustering analysis in each simulation frame. In the second step of the analysis, a cell was considered to be detached if it was separated from the bulk (the biggest cluster) for at least 5 consecutive frames. For each detachment event we saved the x,y coordinates of detachment, the cell ID, timestep to be used for further analysis (eg. analysis relating the detaching events to interface properties in Fig. 3c,d, and local pillar positions Fig. 4d).

The shape of the cellular interface (eg. Fig. 2d,e, Fig. 3a, Fig. 4a) was analyzed by first computing the Delaunay triangulation (convex hull) of cellular positions was in each simulation frame. The Delaunay triangulation was then filtered using the alpha shape algorithm[79] (alphashape library in Python) to determine the concave hull of the cellular interface (alpha = 0.6). The positions of interface cells were subsequently used in the roughness scaling analysis (Fig. 2e, Supplementary Fig. 3c,e) and their connectivity in the analysis of interface shape, perimeter and curvature (Fig. 3a,c,d,h, Fig. 4b, Supplementary Fig. 3a). The local maxima and minima of cell interface were analyzed using the argrelextrema function in SciPy library[80], and the transient protrusions on the order of cell size (protrusion length = average distance to next local minima < 1 *L*) were filtered out.

The interface roughness (Fig. 2e, Supplementary Fig. S3c,e) was quantified using the height function *h(y)*, i.e. the level of invasion of cells in different points of the interface (polar coordinates were used in case of pillar pattern experiments). We analyze the increase of roughness in time by computing interface width *w(l,t)* measuring the root mean square deviations of an interface about its mean value, defined as

$$\mathrm{w(l,t)} = \left\{\frac{1}{N}\sum_{i-1}^{N}\left[(h(y,t) - \bar{h}(t)\right]^2\right\}_{L_{int}}^{1/2}$$

where L_{int}=1000 μm is the length of the interface contour. These fluctuations grow in time in a power law fashion $\mathrm{w(l,t)} \sim t^{\beta}$, with a characteristic critical growth exponent β[31].

The analysis of local heterogeneity of pillars (Fig. 4h, Supplementary Fig. 4e,f) was performed by identifying all close pillars around a given x,y position in disordered pattern (r_{max}= 3.18 *L*, i.e. 3 times average pore size) and dividing them into 4 quadrants (front, back, left right, Fig. 4g). The identified pillars in each quadrant were subsequently weighted by their distance from the reference position $(r_{max}-r)/r_{max}$ and summed.

639

Supplementary Figures

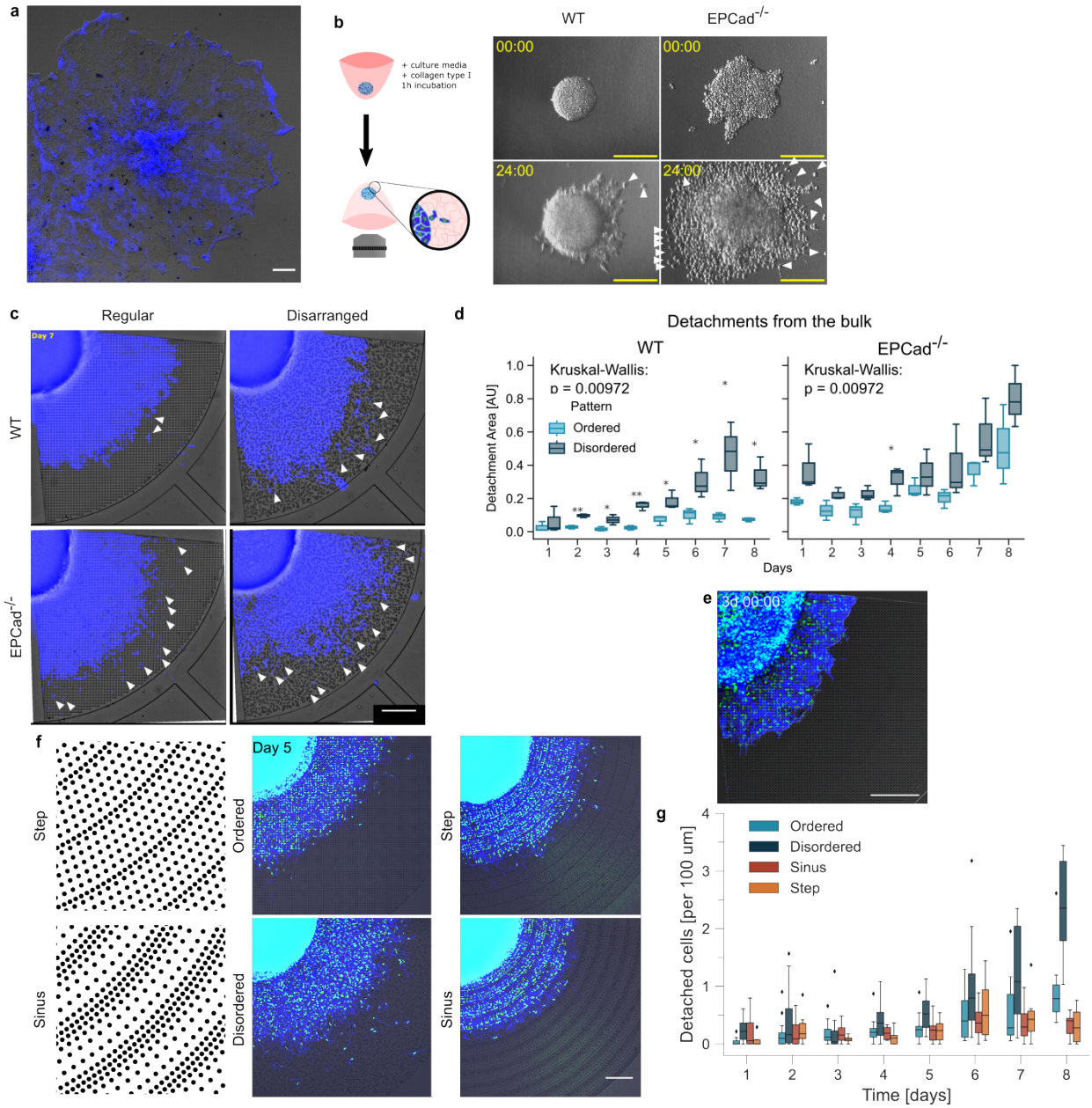

Supplementary Fig. 1: Invasion dynamics of cells in different environments a. 2D invastion assay of WT A431 cells with and without mCherry reporter with 1:10 mix respectively. **b.** Collagen invasion assay of WT and E-,P-Cad$^{-/-}$ spheroids imaged with brightfield microscopy. **c.** Detachments of the WT and E-,P-Cad$^{-/-}$ cells invading into ordered and disordered pillar patterns. White arrows indicate individual detached cells or cell clusters. **d.** Detached cell area in the respective pillar patterns for A431 WT and E-,P-CadKO cells. Scale bars: 100 µm, box and whiskers plot displays median, 1st and 3rd quartiles (hinges) and bars display 1.5 interquartile range from the hinges, n=3 experiments per genotype and pattern followed over 8 days. **e-f.** Cell invasion assays into smaller (6 µm) sized ordered pillar pattern (d) and step-

wise or sinusoidal pattern (e). **g.** Quantified number of detachments for each pillar patterns, where box and whiskers plot displays median, 1st and 3rd quartiles (hinges) and bars display 1.5 interquartile range from the hinges, n=3 experiments per genotype and pattern followed over 8 days. All scale bars: 200μm.

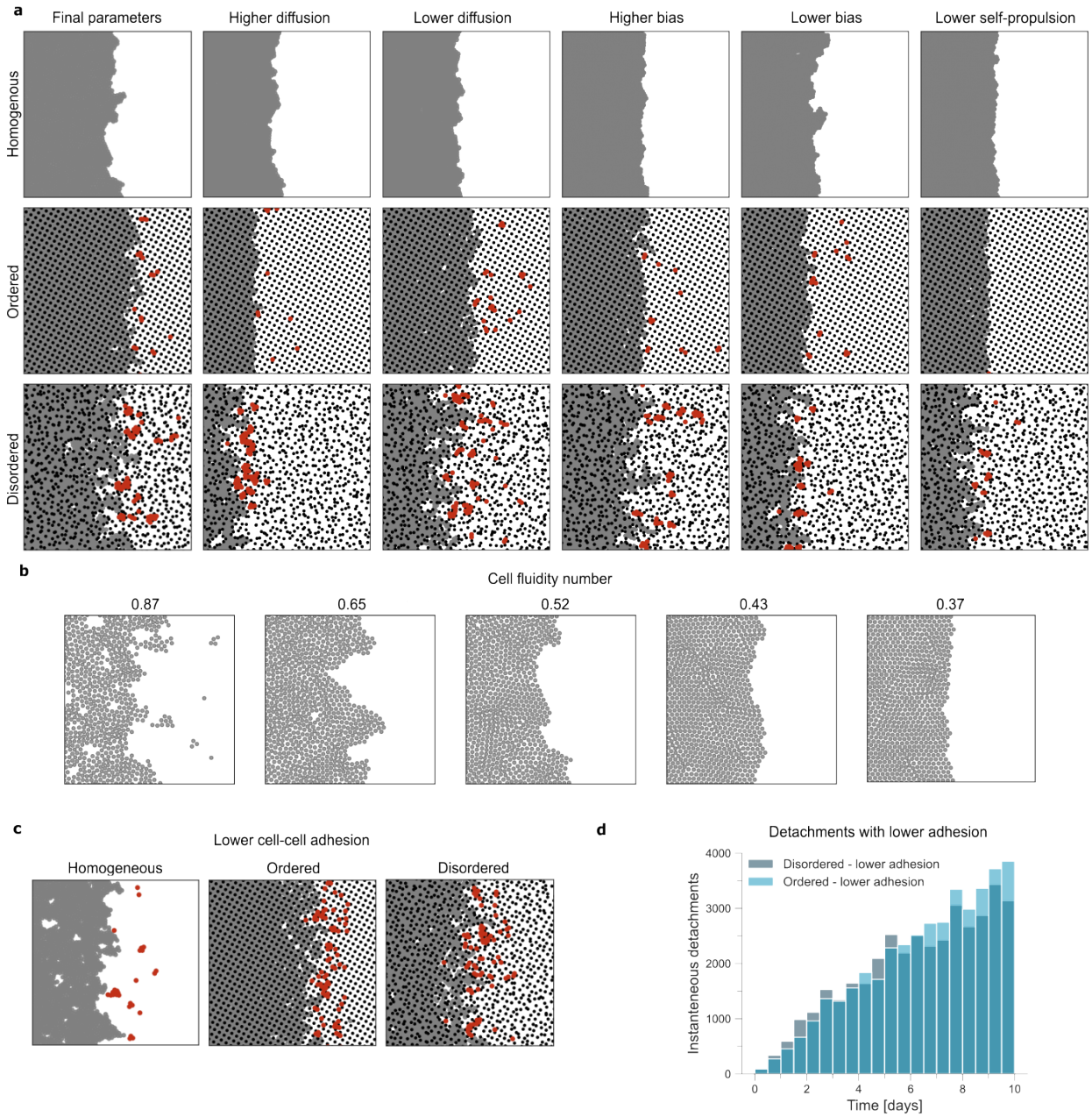

Supplementary Figure 2: Phase diagram of invasion dynamics for different model parameters. a. Temporal increase in detachment rate is a robust phenomenon present both in ordered and disordered pillar patterns, as well as for different simulation parameters. The simulation snapshots show a representative state of the systems at day 6 (cells are shown as grey and pillar as black beads, detached cells are highlighted in red), with the best-fit set of simulation parameters used in the main text (left column, see also

Supplementary Table 1). Each subsequent column shows the effect of changing a single simulation parameter (D_r = 1 τ^{-1}, D_r = 0.5 τ^{-1}, k_{bias} = 0.5 rad/τ, k_{bias} = 1 rad/τ, v_0 = 0.24 L/τ respectively). **b.** Snapshots of simulation of cells in homogeneous environments (grey beads shown with smaller diameter for clarity, day 6), for different values of the fluidity number. High fluidity number (left) leads to numerous detachments, something not observed in wild-type experiments, while low fluidity (right) leads to a solid-like rheology without any re-arrangements on the time scale of the simulations (also not observed). **c.** Snapshots from simulations of cells with lower cell-cell adhesion, corresponding to E-,P-Cad$^{-/-}$ cells (fluidity 0.87, cells are shown as grey and pillar as black beads, detached cells are highlighted in red). This leads to detachments even in the absence of any pillars, i.e. to a much weaker sensitivity to the environment, as seen experimentally. **d.** Quantification for the increase of detachments when lowering the cell-cell adhesion, for either ordered or disordered pillar patterns, showing that the difference between ordered and disordered pattern disappears compared to intermediate adhesion/fluidity.

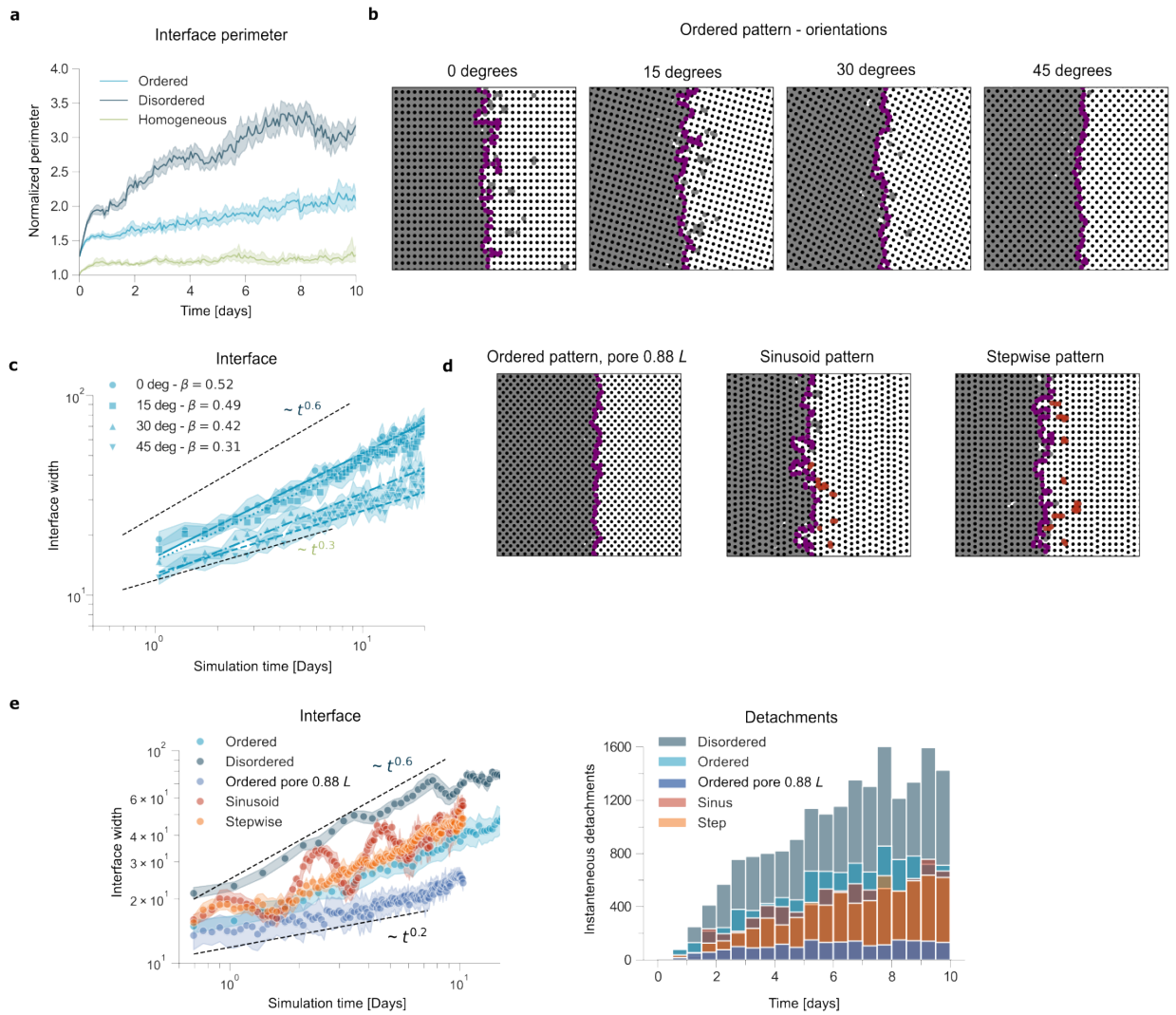

Supplementary Figure 3: Sensitivity analysis of simulation outputs for different pillar patterns. a. Temporal evolution of the interface perimeter, quantified in simulations (n=40 simulations, the shaded intervals indicate standard error). **b.** Differences in invasion behavior with different orientations of regular pattern (snapshots of day 4, cells are shown as grey and pillar as black beads, magenta line represents cell interface). We used the average results of the 4 shown orientations for comparing regular pattern with other geometries, given that invasion is radial in experiments. **c.** Interfacial roughness and roughness exponents in 4 orientations of regular patterns (corresponding to b) (n=10 simulations each, the shaded intervals correspond to standard error). **d.** Simulation snapshots of invasion in sinusoid and stepwise pillar patterns, exhibiting lower or comparable detachments, as in ordered pattern, as seen experimentally in Supplementary Fig 1e-g. Cells are represented as grey and pillars as black beads, detached cells are marked red, cell interface in magenta, day 4. **e.** Quantifications of interface width and detachment numbers in simulations of panel d, showing that it follows a stepwise trend corresponding to the pillar pattern, and that some cells tend to reattach to the bulk resulting in lower overall number of detachments.

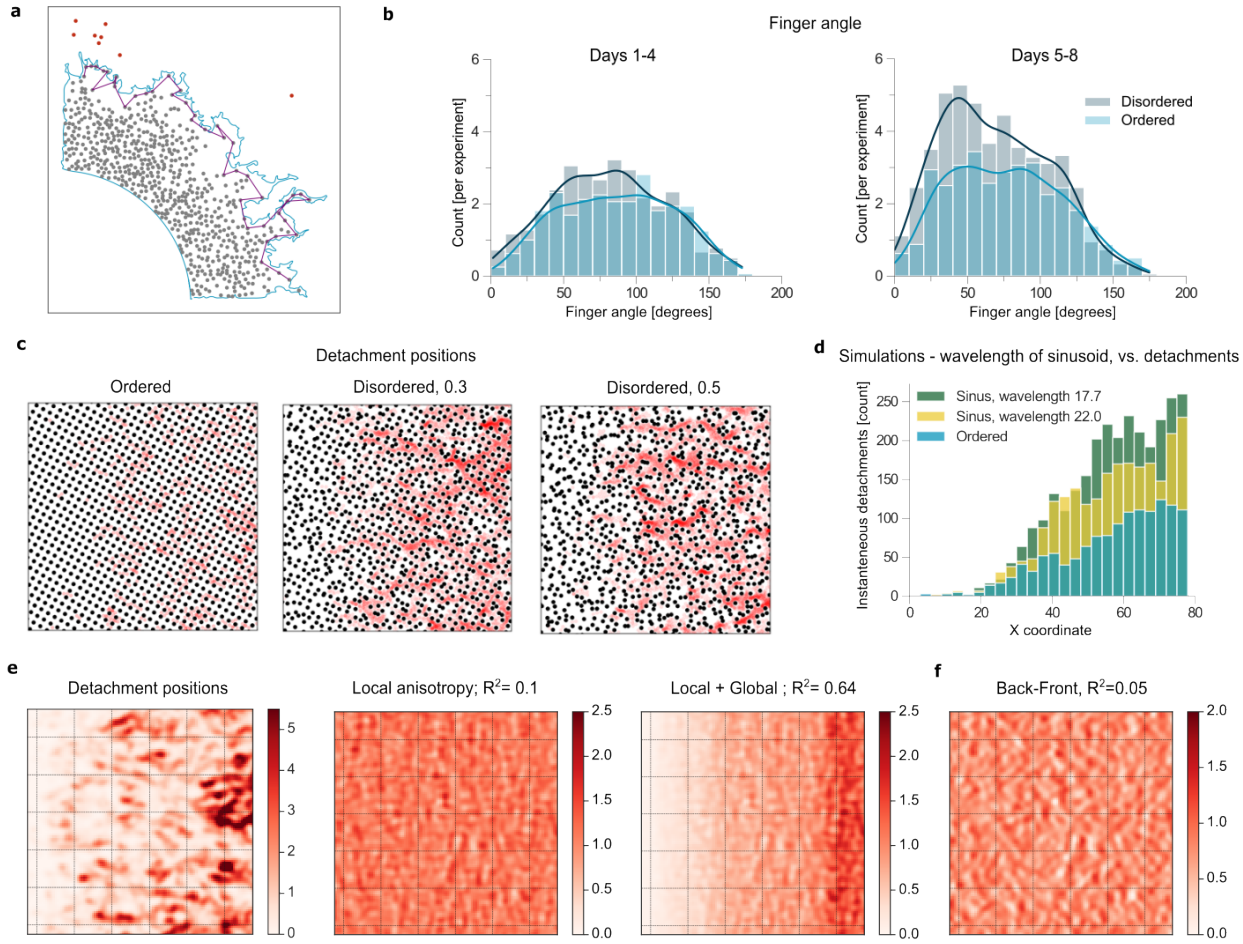

Supplementary Figure 4: Detachments statistics in data and simulations. **a.** Analysis of interface roughness in experiments. The blue line represents the segmented outline of cell bodies and magenta line connects the cell nuclei along the interface, which are used for subsequent roughness and interface curvature analysis (see Methods). **b.** Difference between the finger angle (defined as the angle between the tip of finger and neighboring local minima, with small angles thus corresponding to sharp fingers, see Fig. 3e) of the protrusions in ordered and disordered patterns, which becomes more pronounced in later timepoints (n=16 experiments for regular and n=18 for disordered pattern). **c.** Distribution of detachment events in simulations with increasing disorder in pillar positions (color coded in red for increasing probability). **d.** Temporal increase of detachments in perpendicular sinusoid simulations with smaller wavelength (see Fig. 4a). **e.** Heat map of detachment positions compared to the local anisotropy of pillar positions in disordered pattern (Metric: Left + Right – Front, R^2 = 0.1) and local anisotropy of pillar positions multiplied by the mask, which takes into account the increase of detachments in the direction of invasion (R^2=0.63). detachments analyzed from n=10 simulations. **f.** Example of a different metric calculated using the same analysis (Back-Front), which exhibited lower spatial correlation with detachment positions.

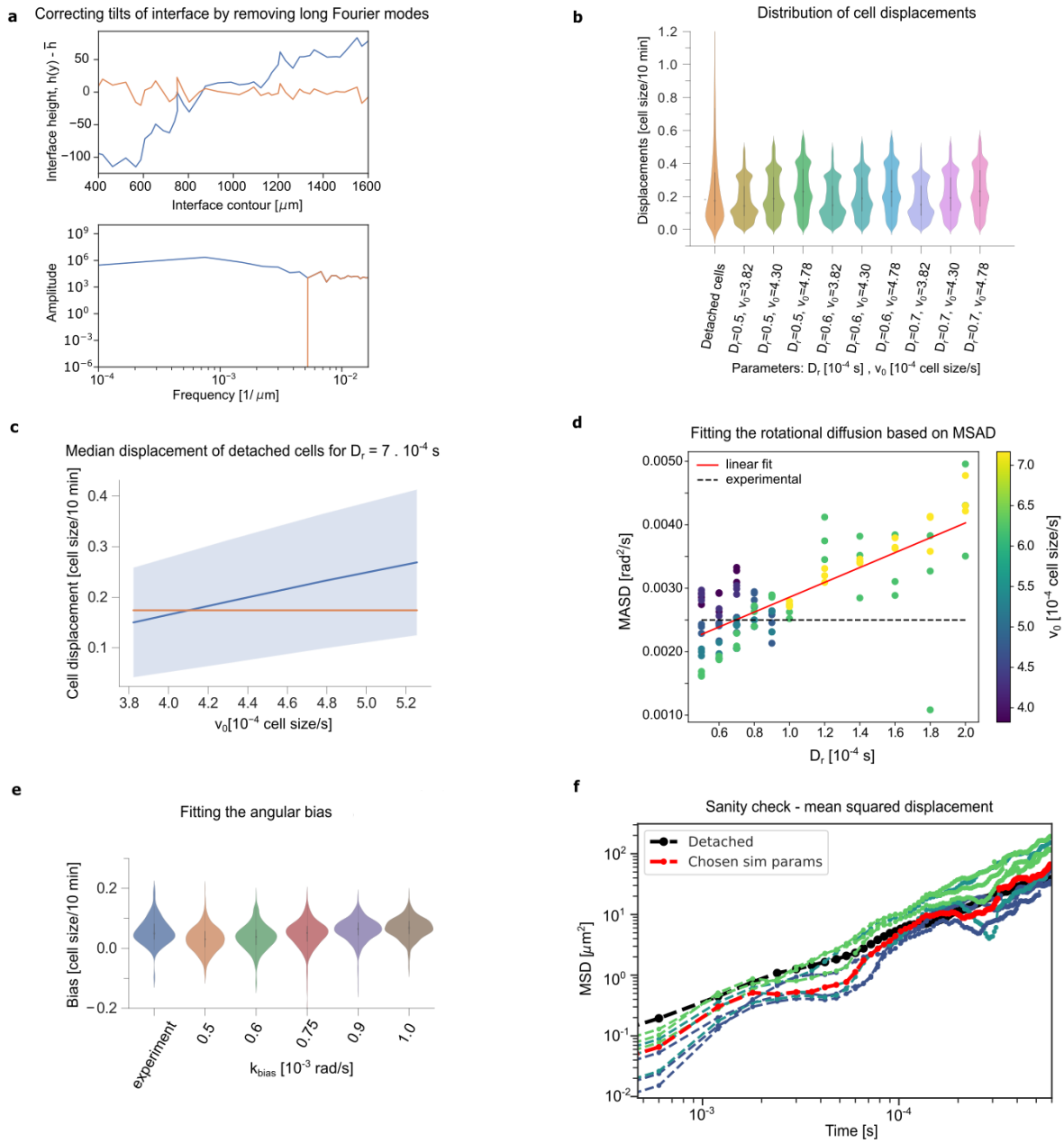

Supplementary Figure 5: Fitting procedure for different model parameters. a) Correction of tilts in the detected experimental interface (blue line) by removing long Fourier modes (orange line). **b-c)** Fitting the active force v_0 based on displacements of single detached cells in a pillar patterns, respectively (experimental data shown in the first two columns of panel b, orange line in panel c represents the median of distribution of detached cells, n=91 trajectories from n=6 experiments). The displacements do not depend on D_r and grow linearly with v_0 (further columns in panel b show n=3 simulations of n=100 sparsely added single cells in ordered pillar patterns with pore size 1.06 *L* and different combinations of parameters). By

comparing the data to different values of v_0, we constrained v_0=0.43 L/τ as the best-fit parameter used in the rest of the simulations unless explicitly mentioned **d)** Fitting of the rotational diffusion constant based on MSAD of single detached cells in a regular pillar pattern (color coded according to value of v_0, black dashed line represents MSAD of detached cells in experiment). As above, we compared the experimental results from trajectories of detached cells to simulations with different rotational diffusion coefficients D_r. We found that the best-fit occurred for 0.7 τ^{-1}, which we use for the rest of the paper unless explicitly mentioned. **e)** Fitting of the k_{bias} based on the radial bias in trajectories of single detached cells in a regular pillar pattern (same procedure as above). We found that k_{bias}=0.75 rad/τ reproduced best the data, which we use for the rest of the paper unless explicitly mentioned. **f)** MSD comparing the detached cells in pillar patterns in experiment and final simulation parameters D_r, v_0, and k_{bias}, chosen according to **b-e**.

725 **Supplementary Table 2.** Interface roughness of cells invading in ordered and disordered patterns in dif-
726 ferent parameter combinations (green – exponents from 0.25-0.44, blue – larger than 0.55).

Pore size	D_r [τ^{-1}]	Ordered pattern *fluidity*				Disordered pattern *fluidity*			
		0.44	**0.52**	**0.60**	**0.76**	**0.44**	**0.52**	**0.60**	**0.76**
0.88 *L*	**0.5**	0.27	0.33	0.41	0.50	0.55	0.70	0.70	0.57
	1	0.19	0.36	0.43	0.44	0.45	0.65	0.72	0.71
	2	0.37	0.25	0.23	0.37	0.44	0.36	0.39	0.49
1.06 *L*	**0.5**	0.48	0.57	0.62	0.59	0.54	0.62	0.78	0.57
	1	0.30	0.45	0.52	0.55	0.44	0.69	0.64	0.59
	2	0.34	0.23	0.28	0.42	0.35	0.32	0.40	0.43
1.24 *L*	**0.5**	0.32	0.32	0.38	0.38	0.57	0.66	0.80	0.49
	1	0.37	0.46	0.49	0.50	0.58	0.69	0.64	0.59
	2	0.33	0.27	0.31	0.41	0.56	0.33	0.40	0.43

727

728 **Supplementary Table 3:** Behavior of the cell bulk in homogeneous environment in simulations with differ-
729 ent parameters (green – KPZ scaling, yellow – KPZ scaling with holes and detachments, red – jammed,
730 collective movement; brown – jammed, no movement

D_r [τ^{-1}]	fluidity					
	0.36	**0.44**	**0.52**	**0.60**	**0.68**	**0.76**
0.1						
0.5						
1						
2						
3						
10						

731

732 # Supplementary Movie Legends

733 **Supplementary Movie 1:** Invasion of A431 human skin carcinoma cells in ordered vs. disordered environ-
734 ments. Cells express cytoplasmic mCherry (blue) and nuclear H2B-GFP (green).

735 **Supplementary Movie 2:** Invasion of A431 human skin carcinoma cells in free environments. Cells express
736 cytoplasmic mCherry (blue) and nuclear H2B-GFP (green).

737 **Supplementary Movie 3:** Invasion of EPCad$^{-/-}$ A431 human skin carcinoma cells in ordered vs. disordered
738 environments. Cells express cytoplasmic mCherry (blue) and nuclear H2B-GFP (green).

739 **Supplementary Movie 4:** Simulations of cells with different fluidity number (i.e. with varying cell-cell inter-
740 action strength) in homogeneous environment showing different level of cell rearrangements. Cells are
741 represented as grey beads.

742 **Supplementary Movie 5:** Simulations of cells migrating in different environments (homogeneous, ordered
743 and disordered. Cells are represented as grey and pillars as black beads.

744 **Supplementary Movie 6:** Simulations of EPCad$^{-/-}$ cells (lower cell-cell adhesion) invading different types
745 of environments. Simulations of cells migrating in different environments (homogeneous, ordered and dis-
746 ordered. Cells are represented as grey and pillars as black beads.

747 **Supplementary Movie 7:** Simulations of cell invasion in spatially structured environments which do not
748 increase detachment rate (regular with smaller pore, sinusoid, stepwise). Cells are represented as grey and
749 pillars as black beads.

750 **Supplementary Movie 8:** Simulation and experiment of cell invasion in sinusoid perpendicular pattern,
751 which creates localized interface protrusions and detachments. Cells in experiment express cytoplasmic
752 mCherry (blue) and nuclear H2B-GFP (green). Cells in simulations are represented as grey and pillars as
753 black beads.

754

755 # References

756 1. Almendro, V., Marusyk, A. & Polyak, K. Cellular heterogeneity and molecular evolution in
757 cancer. *Annu. Rev. Pathol.* **8**, 277–302 (2013).
758 2. Altschuler, S. J. & Wu, L. F. Cellular Heterogeneity: Do Differences Make a Difference? *Cell*
759 **141**, 559–563 (2010).
760 3. McGranahan, N. & Swanton, C. Clonal Heterogeneity and Tumor Evolution: Past, Present,
761 and the Future. *Cell* **168**, 613–628 (2017).
762 4. Cheung, K. J. & Ewald, A. J. A collective route to metastasis: Seeding by tumor cell clusters.
763 *Science* **352**, 167–169 (2016).
764 5. Yang, R. *et al.* Distinct epigenetic features of tumor-reactive CD8+ T cells in colorectal can-
765 cer patients revealed by genome-wide DNA methylation analysis. *Genome Biol.* **21**, 2
766 (2019).

767 6. Ferguson, L. P., Diaz, E. & Reya, T. The Role of the Microenvironment and Immune System
768 in Regulating Stem Cell Fate in Cancer. *Trends Cancer* **7**, 624–634 (2021).
769 7. Friedl, P. & Alexander, S. Cancer Invasion and the Microenvironment: Plasticity and Reci-
770 procity. *Cell* **147**, 992–1009 (2011).
771 8. Spill, F., Reynolds, D. S., Kamm, R. D. & Zaman, M. H. Impact of the physical microenviron-
772 ment on tumor progression and metastasis. *Curr. Opin. Biotechnol.* **40**, 41–48 (2016).
773 9. Giampieri, S. *et al.* Localized and reversible TGFβ signalling switches breast cancer cells
774 from cohesive to single cell motility. *Nat. Cell Biol.* **11**, 1287–1296 (2009).
775 10. Brabletz, T. EMT and MET in Metastasis: Where Are the Cancer Stem Cells? *Cancer Cell*
776 **22**, 699–701 (2012).
777 11. Padmanaban, V. *et al.* E-cadherin is required for metastasis in multiple models of breast
778 cancer. *Nature* 1–6 (2019) doi:10.1038/s41586-019-1526-3.
779 12. Rezk, R. *et al.* Spatial heterogeneity of cell-matrix adhesive forces predicts human glioblas-
780 toma migration. *Neuro-Oncol. Adv.* **2**, vdaa081 (2020).
781 13. Flommersfeld, J., Stöberl, S., Shah, O., Rädler, J. O. & Broedersz, C. P. Geometry-Sensi-
782 tive Protrusion Growth Directs Confined Cell Migration. *Phys. Rev. Lett.* **132**, 098401
783 (2024).
784 14. Jouybar, M., Sleeboom, J. J. F., Vaezzadeh, E., Sahlgren, C. M. & den Toonder, J. M. J. An
785 in vitro model of cancer invasion with heterogeneous ECM created with droplet microfluid-
786 ics. *Front. Bioeng. Biotechnol.* **11**, (2023).
787 15. Wang, W., Law, R. A., Perez Ipiña, E., Konstantopoulos, K. & Camley, B. A. Confinement,
788 Jamming, and Adhesion in Cancer Cells Dissociating from a Collectively Invading Strand.
789 *PRX Life* **3**, 013012 (2025).
790 16. Bocanegra-Moreno, L., Singh, A., Hannezo, E., Zagorski, M. & Kicheva, A. Cell cycle dy-
791 namics controls fluidity of the developing mouse neuroepithelium. 2022.01.20.477048 Pre-
792 print at https://doi.org/10.1101/2022.01.20.477048 (2022).

17. Mongera, A. *et al.* A fluid-to-solid jamming transition underlies vertebrate body axis elongation. *Nature* (2018) doi:10.1038/s41586-018-0479-2.
18. Petridou, N. I., Corominas-Murtra, B., Heisenberg, C. P. & Hannezo, E. Rigidity percolation uncovers a structural basis for embryonic tissue phase transitions. *Cell* **184**, 1914-1928.e19 (2021).
19. Pinheiro, D., Kardos, R., Hannezo, É. & Heisenberg, C.-P. Morphogen gradient orchestrates pattern-preserving tissue morphogenesis via motility-driven unjamming. *Nat. Phys.* **18**, 1482–1493 (2022).
20. Bi, D., Lopez, J. H., Schwarz, J. M. & Manning, M. L. A density-independent rigidity transition in biological tissues. *Nat. Phys.* **11**, 1074–1079 (2015).
21. Mitchel, J. A. *et al.* In primary airway epithelial cells, the unjamming transition is distinct from the epithelial-to-mesenchymal transition. *Nat. Commun.* **11**, 1–14 (2020).
22. Kato, T. *et al.* Interplay of adherens junctions and matrix proteolysis determines the invasive pattern and growth of squamous cell carcinoma. *eLife* **12**, e76520 (2023).
23. Grosser, S. *et al.* Cell and Nucleus Shape as an Indicator of Tissue Fluidity in Carcinoma. *Phys. Rev. X* **11**, (2021).
24. Ilina, O. *et al.* Cell–cell adhesion and 3D matrix confinement determine jamming transitions in breast cancer invasion. *Nat. Cell Biol.* **22**, 1103–1115 (2020).
25. Malinverno, C. *et al.* Endocytic reawakening of motility in jammed epithelia. *Nat. Mater.* **16**, 587–596 (2017).
26. Oswald, L., Grosser, S., Smith, D. M. & Käs, J. A. Jamming transitions in cancer. *J. Phys. Appl. Phys.* **50**, 483001 (2017).
27. Fuhs, T. *et al.* Rigid tumours contain soft cancer cells. *Nat. Phys.* **18**, 1510–1519 (2022).
28. Frittoli, E. *et al.* Tissue fluidification promotes a cGAS–STING cytosolic DNA response in invasive breast cancer. *Nat. Mater.* (2022) doi:10.1038/s41563-022-01431-x.

29. Kardar, M., Parisi, G. & Zhang, Y.-C. Dynamic Scaling of Growing Interfaces. *Phys. Rev. Lett.* **56**, 889–892 (1986).
30. Muzzio, N. E., Pasquale, M. A., González, P. H. & Arvia, A. J. Influence of individual cell motility on the 2D front roughness dynamics of tumour cell colonies. *J. Biol. Phys.* **40**, 285–308 (2014).
31. Brú, A., Albertos, S., Luis Subiza, J., García-Asenjo, J. L. & Brú, I. The Universal Dynamics of Tumor Growth. *Biophys. J.* **85**, 2948–2961 (2003).
32. Maunuksela, J. *et al.* Kinetic Roughening in Slow Combustion of Paper. *Phys. Rev. Lett.* **79**, 1515–1518 (1997).
33. Takeuchi, K. A. & Sano, M. Evidence for Geometry-Dependent Universal Fluctuations of the Kardar-Parisi-Zhang Interfaces in Liquid-Crystal Turbulence. *J. Stat. Phys.* **147**, 853–890 (2012).
34. Giard, D. J. *et al.* In vitro cultivation of human tumors: establishment of cell lines derived from a series of solid tumors. *J. Natl. Cancer Inst.* **51**, 1417–1423 (1973).
35. Macpherson, I. R. *et al.* p120-catenin is required for the collective invasion of squamous cell carcinoma cells via a phosphorylation-independent mechanism. *Oncogene* **26**, 1210334 (2007).
36. Bertillot, F., Miroshnikova, Y. A. & Wickström, S. A. SnapShot: Mechanotransduction in the nucleus. *Cell* **185**, 3638-3638.e1 (2022).
37. Kalukula, Y., Stephens, A. D., Lammerding, J. & Gabriele, S. Mechanics and functional consequences of nuclear deformations. *Nat. Rev. Mol. Cell Biol.* **23**, 583–602 (2022).
38. Venturini, V. *et al.* The nucleus measures shape changes for cellular proprioception to control dynamic cell behavior. *Science* **370**, eaba2644 (2020).
39. Venturini, V. *et al.* The nucleus as a mechanosensitive controller of cell behavior. *Biophys. J.* **121**, 490a (2022).

40. Lomakin, A. J. *et al.* The nucleus acts as a ruler tailoring cell responses to spatial constraints. *Science* **370**, eaba2894 (2020).
41. Kidiyoor, G. R. *et al.* ATR is essential for preservation of cell mechanics and nuclear integrity during interstitial migration. *Nat. Commun.* **11**, 4828 (2020).
42. Alert, R. & Trepat, X. Physical Models of Collective Cell Migration. *Annu. Rev. Condens. Matter Phys.* **11**, 77–101 (2020).
43. Basan, M., Elgeti, J., Hannezo, E., Rappel, W.-J. & Levine, H. Alignment of cellular motility forces with tissue flow as a mechanism for efficient wound healing. *Proc. Natl. Acad. Sci.* **110**, 2452–2459 (2013).
44. Garcia, S. *et al.* Physics of active jamming during collective cellular motion in a monolayer. *Proc. Natl. Acad. Sci.* **112**, 15314–15319 (2015).
45. Henkes, S., Fily, Y. & Marchetti, M. C. Active jamming: Self-propelled soft particles at high density. *Phys. Rev. E* **84**, 040301 (2011).
46. Family, F. & Vicsek, T. Scaling of the active zone in the Eden process on percolation networks and the ballistic deposition model. *J. Phys. Math. Gen.* **18**, L75 (1985).
47. Chepizhko, O. *et al.* Bursts of activity in collective cell migration. *Proc. Natl. Acad. Sci.* **113**, 11408–11413 (2016).
48. Podewitz, N., Jülicher, F., Gompper, G. & Elgeti, J. Interface dynamics of competing tissues. *New J. Phys.* **18**, 083020 (2016).
49. Rapin, G. *et al.* Roughness and dynamics of proliferating cell fronts as a probe of cell–cell interactions. *Sci. Rep.* **11**, 8869 (2021).
50. Olami, Z., Procaccia, I. & Zeitak, R. Interface roughening in systems with quenched disorder. *Phys. Rev. E* **52**, 3402–3414 (1995).
51. Dias, C. S., Yunker, P. J., Yodh, A. G., Araújo, N. a. M. & Gama, M. M. T. da. Interaction anisotropy and the KPZ to KPZQ transition in particle deposition at the edges of drying drops. *Soft Matter* **14**, 1903–1907 (2018).

52. Csahók, Z., Honda, K., Somfai, E., Vicsek, M. & Vicsek, T. Dynamics of surface roughening in disordered media. *Phys. Stat. Mech. Its Appl.* **200**, 136–154 (1993).

53. Muzzio, N. E. *et al.* Spatio-temporal morphology changes in and quenching effects on the 2D spreading dynamics of cell colonies in both plain and methylcellulose-containing culture media. *J. Biol. Phys.* **42**, 477–502 (2016).

54. Mark, S. *et al.* Physical Model of the Dynamic Instability in an Expanding Cell Culture. *Biophys. J.* **98**, 361–370 (2010).

55. Tarle, V., Ravasio, A., Hakim, V. & Gov, N. S. Modeling the finger instability in an expanding cell monolayer. *Integr. Biol.* **7**, 1218–1227 (2015).

56. Büscher, T., Diez, A. L., Gompper, G. & Elgeti, J. Instability and fingering of interfaces in growing tissue. *New J. Phys.* **22**, 083005 (2020).

57. Dai, W. *et al.* Tissue topography steers migrating Drosophila border cells. *Science* **370**, 987–990 (2020).

58. Park, D. *et al.* Extracellular matrix anisotropy is determined by TFAP2C-dependent regulation of cell collisions. *Nat. Mater.* 1–12 (2019) doi:10.1038/s41563-019-0504-3.

59. Conklin, M. W. *et al.* Aligned Collagen Is a Prognostic Signature for Survival in Human Breast Carcinoma. *Am. J. Pathol.* **178**, 1221–1232 (2011).

60. Mukherjee, A., Jana, A., Koons, B. & Nain, A. Design of Fiber Networks for Studying Metastatic Invasion. in *Biomechanics in Oncology* (eds. Dong, C., Zahir, N. & Konstantopoulos, K.) 289–318 (Springer International Publishing, Cham, 2018). doi:10.1007/978-3-319-95294-9_14.

61. Tsingos, E., Bakker, B. H., Keijzer, K. A. E., Hupkes, H. J. & Merks, R. M. H. Hybrid cellular Potts and bead-spring modeling of cells in fibrous extracellular matrix. *Biophys. J.* **122**, 2609–2622 (2023).

62. Labernadie, A. *et al.* A mechanically active heterotypic E-cadherin/N-cadherin adhesion enables fibroblasts to drive cancer cell invasion. *Nat. Cell Biol.* **19**, 224–237 (2017).

63. Leithner, A. *et al.* Diversified actin protrusions promote environmental exploration but are dispensable for locomotion of leukocytes. *Nat. Cell Biol.* **18**, 1253–1259 (2016).

64. Schindelin, J. *et al.* Fiji: an open-source platform for biological-image analysis. *Nat. Methods* **9**, 676–682 (2012).

65. Tinevez, J.-Y. *et al.* TrackMate: An open and extensible platform for single-particle tracking. *Methods* **115**, 80–90 (2017).

66. Linkert, M. *et al.* Metadata matters: access to image data in the real world. *J. Cell Biol.* **189**, 777–782 (2010).

67. Berg, S. *et al.* ilastik: interactive machine learning for (bio)image analysis. *Nat. Methods* **16**, 1226–1232 (2019).

68. Agostinelli, C. & Lund, U. *R Package \texttcircular: Circular Statistics (Version 0.4-95)*. (CA: Department of Environmental Sciences, Informatics and Statistics, Ca' Foscari University, Venice, Italy. UL: Department of Statistics, California Polytechnic State University, San Luis Obispo, California, USA, 2022).

69. Pewsey, A., Neuhäuser, M. & Ruxton, G. D. *Circular Statistics in R*. (OUP Oxford, 2013).

70. Howse, J. R. *et al.* Self-Motile Colloidal Particles: From Directed Propulsion to Random Walk. *Phys. Rev. Lett.* **99**, 048102 (2007).

71. Shaebani, M. R., Wysocki, A., Winkler, R. G., Gompper, G. & Rieger, H. Computational models for active matter. *Nat. Rev. Phys.* **2**, 181–199 (2020).

72. Anderson, J. A., Glaser, J. & Glotzer, S. C. HOOMD-blue: A Python package for high-performance molecular dynamics and hard particle Monte Carlo simulations. *Comput. Mater. Sci.* **173**, 109363 (2020).

73. Mandal, R., Bhuyan, P. J., Chaudhuri, P., Dasgupta, C. & Rao, M. Extreme active matter at high densities. *Nat. Commun.* **11**, 2581 (2020).

74. Angelini, T. E. *et al.* Glass-like dynamics of collective cell migration. *Proc. Natl. Acad. Sci.* **108**, 4714–4719 (2011).

75. Kang, W. *et al.* A novel jamming phase diagram links tumor invasion to non-equilibrium phase separation. *iScience* **24**, 103252 (2021).

76. Narinder, N., F. Bos, M., Abaurrea-Velasco, C., Graaf, J. de & Bechinger, C. Understanding enhanced rotational dynamics of active probes in rod suspensions. *Soft Matter* **18**, 6246–6253 (2022).

77. Yamashita, H. *et al.* Lysophosphatidic Acid Upregulates Laminin-332 Expression during A431 Cell Colony Dispersal. *J. Oncol.* **2010**, 107075 (2010).

78. Tweedy, L. *et al.* Seeing around corners: Cells solve mazes and respond at a distance using attractant breakdown. *Science* **369**, eaay9792 (2020).

79. Zhou, W. & Yan, H. Alpha shape and Delaunay triangulation in studies of protein-related interactions. *Brief. Bioinform.* **15**, 54–64 (2014).

80. Virtanen, P. *et al.* SciPy 1.0: fundamental algorithms for scientific computing in Python. *Nat. Methods* **17**, 261–272 (2020).